# APPLICATIONS AND OPTIMIZATION OF RESPONSE SURFACE METHODOLOGIES IN HIGH-PRESSURE, HIGH-TEMPERATURE GAUGES

A Thesis
Presented to
The Academic Faculty

by

Santiago Hässig Fonseca

In Partial Fulfillment
of the Requirements for the Degree
Master of Science in the
School of Electrical and Computer Engineering

Georgia Institute of Technology
August 2012

# APPLICATIONS AND OPTIMIZATION OF RESPONSE SURFACE METHODOLOGIES IN HIGH-PRESSURE, HIGH-TEMPERATURE GAUGES

Approved by:

Professor Abdallah Ougazzaden,
Committee Chair
School of Electrical and Computer
Engineering
*Georgia Institute of Technology*

Professor Paul L. Voss, Advisor
School of Electrical and Computer
Engineering
*Georgia Institute of Technology*

Professor Matthieu Bloch
School of Electrical and Computer
Engineering
*Georgia Institute of Technology*

Date Approved: 15 June 2012

*To my father and mother,*

*friends and relatives,*

*and above all,*

*Germano.*

# PREFACE

The use of the pressure gauge in the recovery and production of hydrocarbons dates back to the early 1900s and continues to rank among the most popular tools in well testing:

- In its infant stages, well analysis provided an estimate of well performance, and relied only on rudimentary pressure measurements.
- By the 1980s, improvements in the state-of-the-art techniques led to pressure-derivative analysis, which gave birth to a more detailed parameter estimation for reservoir characterization.
- Most recently, the advent of powerful personal computers, improvements in computer-aided analysis, and the introduction of deconvolution yielded far more reliable interpretation model identification methods through inverse problem solving.

The evolution in well test analysis implies, and goes hand-in-hand with, advancements in pressure gauge technology capable of acquiring richer pressure data. Reservoir models will continue to evolve in complexity, and interpretation requirements will continue to demand greater confidence in the results, vis-à-vis the uncertainty ranges in parameter and model estimation. Therefore, a great deal of focus has been placed in the development of pressure gauges over the last three decades.

## *Improving Measurement Quality*

The well testing community has invested a significant effort in improving gauge resolution, mitigating short- and long-term pressure drifts, and compensating for temperature transient errors. This latter point, that of generating accurate measurements in dynamic pressure environments, is the holy grail in the area of well testing. The arching theme, it goes without saying, is that the industry continues to push toward improved measurement accuracy and reliability.

### *Aligning Multiple Tool Signals*

A seemingly ancillary, albeit significant, issue in downhole measurement accuracy and reliability is that of timing. Generally, well tests require correlating a measurement with a particular timestamp. It follows that well test tools include a timing mechanism, clock, or oscillator. Aging, pressure response hysteresis, and temperature effects contribute to systematic offsets and drifts in quartz-oscillator clocks. Given the non-linear effects of downhole conditions on quartz response, clock drift is a difficult mechanism to rectify, and, when dealing with multiple tools, is typically compensated in an ad-hoc manner by manually aligning pressure events.

### *Modeling Tool Autonomy*

Not all research efforts are focused on measurement quality. Another area of development is that of downhole tool lifetime, or autonomy. Downhole measurement tools can be powered in a number of ways – e.g., via drill string, a downhole power generator, or a battery pack. In the last example, autonomy becomes a principal concern. Battery packs are expensive, are not necessarily reusable, present a potential chemical/explosive hazard, and power the tools for a limited amount of time relative to other powering methods. The silver lining is their portability and ease-of-use when deployed in the field. But the variability in manufacturing, the cost incurred in testing these batteries, and the time it requires to deplete them are compounding reasons

for the current lack of verified autonomy models.

The leitmotif of the oil services' future is in *real-time*: monitoring, interpretation, and decision-making. These are "modern" services that may lead the well testing industry once they mature and become a standard, but this evolution must accompany continued improvement in tool reliability, data quality, and remote autonomy.

# ACKNOWLEDGEMENTS

This work was sponsored by the Schlumberger (SLB) Masters Fellowship through the Georgia Tech - Lorraine (GTL) Graduate Program. Thanks to GTL for bringing me to France for the duration of my studies. I enjoyed an amazing year in the city of Metz. A special thanks to Schlumberger for hosting and funding my research in Paris.

A very special thanks to Dr. Bertrand Boussert, Karim Mekouar, and John Fritsch for inviting me to GTL/SLB and supporting me throughout the Fellowship. An elaborate "Thank You" to my thesis committee: Dr. Abdallah Ougazzaden for teaching and comprising more than half of my degree, Dr. Matthieu Bloch for not shunning me after I switched out of Information Theory, and Dr. Paul Voss for kindly accepting to be my advisor from the beginning, and for organically guiding me throughout the (at times) inorganic evolution of this thesis.

The research at the Riboud Product Center would have been impossible without the guidance and support of Sylvain Petithomme, who patiently addressed the innumerable questions I had in the areas of pressure gauge engineering and commercialization. For helping me understand product marketability and value, I thank Paul Sims. And for endorsing my foray into SLB's scientific community and providing a forum that welcomed (read: questioned) my research, I give a very special thanks to Dr. Martin Lüling.

Merci à l'equipe du Bât 5 et 7: David Hoyle, James Gillian, Alain Buisson, Eric Parot, Dr. Yoann Jaffre, Clio Fouque, Laurent Cotelle, Elias Temer, et Veronique Gerber.

Dedico esta tesis a mi familia.

# TABLE OF CONTENTS

# LIST OF TABLES

# LIST OF FIGURES

# LIST OF SYMBOLS OR ABBREVIATIONS

| | |
|---|---|
| **Atm** | Atmospheric pressure. |
| $CI$ | Confidence Interval. |
| **DP** | Dynamic programming. |
| **DST** | Drill stem test. |
| **DTW** | Dynamic time warp. |
| **DUT** | Device Under Test. |
| **DWT** | Dead-Weight Tester. |
| **EOL** | End of Life. |
| **FS** | Full-Scale (of tool rating). |
| **HPHT** | High-Pressure, High-Temperature. |
| $MQD$ | Mean quadratic deviation. |
| $P_c$ | Computed pressure. |
| $P_e$ | Experimental pressure. |
| **psi** | Pound per square inch. |
| **RIH** | Run in Hole. |
| $S_p$ | Pressure sensor frequency. |
| $S_t$ | Temperature sensor frequency. |
| **THQR** | HPHT Quartz Recorder. |

# SUMMARY

This body of work comprises a series of improvements in calibration, operation, and signal processing of high-pressure, high-temperature (HPHT) quartz memory gauges that are typically used in oil well testing. The gauge calibration process is introduced in Chapter 2 to provide a context for the application of the unpaired sample t-test methodology; new gauge metrology is verified with field data. In Chapter 3, calibration multivariate regression is detailed and four sets of calibration points are compared to compute the set that produces the greatest gauge accuracy. Chapter 4 provides the theory and implementation of a dynamic time warp algorithm to align memory gauge signals. Finally, Chapter 5 develops an empirical model for tool autonomy and proposes future battery autonomy test campaigns to improve the model. Specific contributions of this work include:

- Application of the unpaired sample statistical t-test to quartz sensor calibration. This metrological methodology reduces uncertainty in gauge metrology, improving absolute tool accuracy by 33% and relative tool accuracy (i.e., in gradient measurements) by 56%.

- Improvement of gauge accuracy by removing calibration points that emulate unlikely downhole conditions – i.e., low pressure at all temperatures, and high pressure at low temperatures. In addition to reducing calibration time by a factor of 1.3, there is a reduction of 14.1% in calibrated gauge's mean quadratic deviation.

- Implementation of a dynamic time warp algorithm that accounts for relative clock drifts, time shifts, and non-linear misalignments between 2+ gauges. The

effectiveness of the algorithm is limited only by the sampling clock time resolution, and yields computational results that vastly exceed conventional manual, qualitative alignment procedures.

- Empirical modeling of tool autonomy based on gauge selection, battery pack, sampling mode, and average well temperature. A first of its kind, the model distills autonomy into two independent parameters, each a function of the same two orthogonal factors: battery power capacity and gauge current consumption as functions of sampling mode and well temperature – a premise that, for 3+ gauge and battery models, reduces the design of future autonomy experiments by at least a factor of 1.5.

# CHAPTER I

# INTRODUCTION

At the turn of the 20th century, oil exploration started to pick up almost exclusively in shallow wells. The production in such wells typically consisted of an ad-hoc installation of pulleys on a wooden structure (the forefather of the modern "christmas tree" pressure manifold) and extraction was performed by means of a literal bucket. As history would show, hydrocarbon exploration would continue to grow, shallow reservoirs would deplete, and deep drilling would become the standard. The challenges in deep drilling, compounded with the increasing demand for hydrocarbons (namely oil), set the stage for the evolution of drilling technology over the 20th and 21st centuries. Figure 1 provides a snapshot of this evolution: a pressure manifold has replaced 5 speculators, an oil man, and a mule.

The palette of modern well testing tools is vast, with an impressive technological offering that ranges from simple pressure, temperature, and resistivity logging, to ultrasonic scanning, in situ fluid sampling, and nuclear magnetic resonance. For as relatively simple as pressure gauge technology may seem, it has consistently thrived as a top service in reservoir characterization. Short of sharing history with the mule in Figure 1(a), gauges have witnessed the technological evolution of oil exploration from its onset.

## *1.1 Reservoir Interpretation*

The theory and mechanics behind reservoir characterization are not essential to understanding pressure gauge technology. Only a brief overview of characterization parameters and pressure/flow tests is included to provide some context for the remainder of the presented work. However, for the interested reader, Horne provides

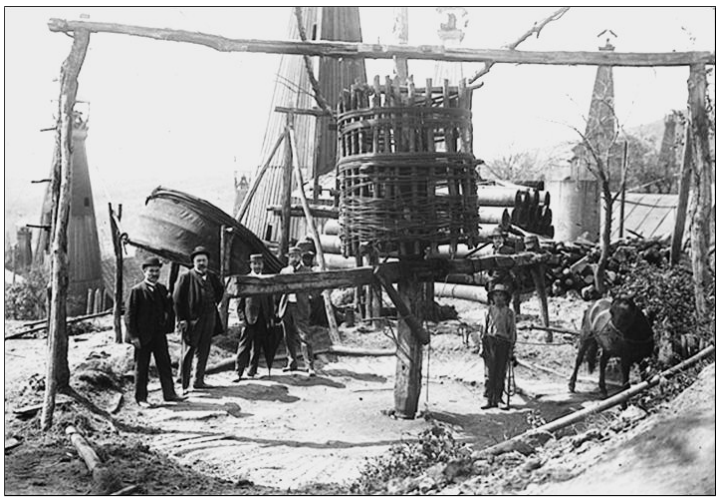

(a) Mule-Operated Pulley (circa 1910)

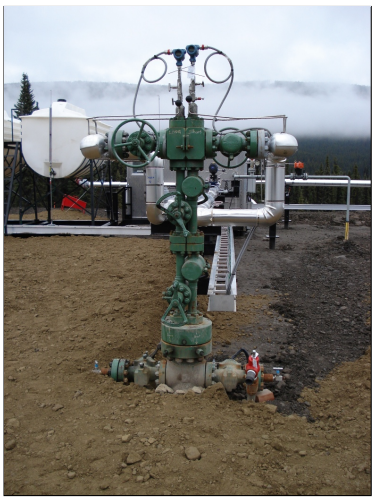

(b) Modern "Christmas Tree"

Figure 1: Evolution of oil production over the span of one hundred years. The mule-operated pulley in (a) and the "tree" in (b) are methods of managing oil flow out of the well.

an in-depth treatment of modern well test analysis [16]. This section draws heavily from his introduction to reservoir characterization.

### 1.1.1 Reservoir Characterization

A reservoir behaves like a "black box" whose characterization is limited to measured output responses to input stimuli – for instance, relating a pressure transient output to a flow rate transient input. The task of reservoir interpretation, which is based on selecting a model that explains the output/input relationship, is known as an inverse problem in which model parameters must be inferred, rather than directly measured. This is a problem that rarely has a unique solution, and therefore the solution space is often minimized by focusing attention on reservoir models that are contextually suitable.

Horne breaks down pressure transient analysis into three functional categories: reservoir evaluation, reservoir management, and reservoir description. The first, reservoir evaluation, is the basis for calculating the productive capacity of the well, which in turn helps determine if the reservoir is solvent. Once a reservoir has been selected

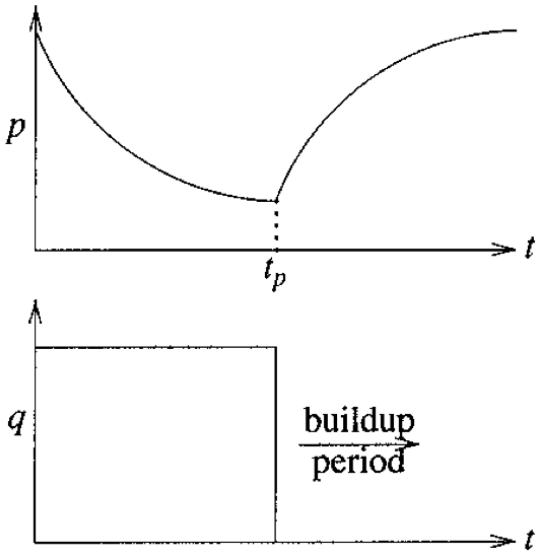


Figure 2: Pressure ($p$) buildup, and constant flow rate ($q$) after shut-in at $t_p$. Illustration borrowed from [16].

for exploration, reservoir management efforts monitor the performance and health of the well. Finally, the task of characterizing the reservoir is a means of forecasting the reservoir performance and, subsequently, establishing a production plan [16].

It is appropriate to note that in the oil business, which is a results-driven, bottom-line industry, the primary goal of evaluating, managing, and describing reservoirs is to maximize profit. Profit, in turn, drives the continued improvement of exploration and production technology. Therefore, from the perspective of the oil technologist, it is important to understand that academic merit alone rarely drives oil research.

### 1.1.2 Well tests

A variety of well tests exist in reservoir evaluation, management, and description. A common well test, and the only one discussed in this work, is that of a pressure buildup, in which the valve on a flowing well is shut (an event referred to as shut-in). The sudden stop in the rate of flow, and subsequent pressure transient buildup, are illustrated in Figure 2.

A slightly more elaborate extension of a buildup is that of drill stem test (DST),

Table 1: Resonant Quartz Sensor Metrology Adapted from [28]

| | Accuracy (% of FS) | Max Temp. (°C) | Press. Range (psi) | Drift Rate/yr |
|---|---|---|---|---|
| Thickness Shear Mode | 0.01 | 175 | 110–16k | $> 7$ psi |
| Vibrating Beams | 0.015 | 150–175 | 100–15k | 1.5–2% |

in which alternating sequences of flows and shut-ins are performed while the pressure is measured by a downhole gauge that has been lowered via a drill string. The pressure profile associated with this measurement campaign will be the focus of the data analyzed in Chapters 2 and 4.

## *1.2 Basics of the Quartz Pressure Gauge*

Pressure gauges have been through a long process of evolution, which means that any decent overview of the technology's history would prove a lengthy distraction. For the interested reader, in [28] Omotosho provides a review of downhole sensor technologies, including a section dedicated to the most common sensor in the petroleum industry: the resonant quartz sensor.

Table 1 summarizes characteristics of two types of downhole quartz sensors: the thickness shear-mode sensor and the vibrating beam sensor. The Schlumberger Signature$^{TM}$ quartz gauges, which are the focus of the case studies in Chapters 2, 3, and 5, rely on thickness shear mode technology.

### 1.2.1 Schlumberger Signature$^{TM}$ Gauges

The methods presented in this body of work can be applied to a broad range of processes and technologies (and not just pressure gauges). That said, it is noted that where analysis and case studies required it, Schlumberger's Signature$^{TM}$ line of pressure gauges was used. The line consists of three gauge models that differ in their rated operating temperatures and pressures. Chapters 2 and 3 pay particular

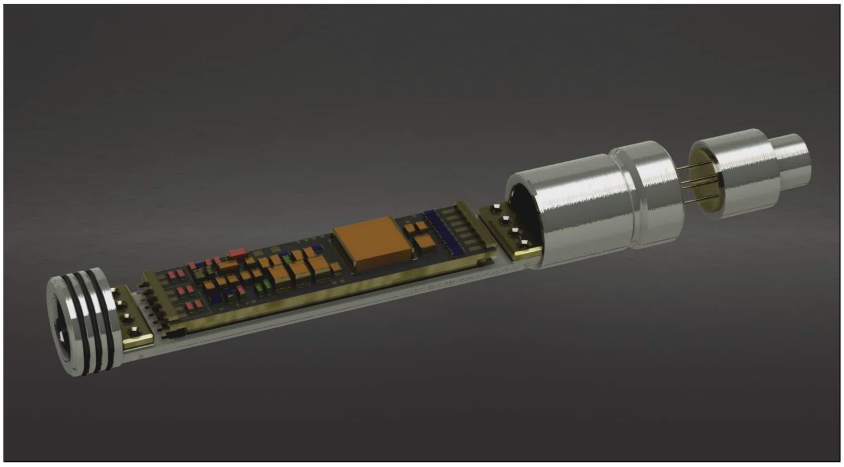

Figure 3: 3D rendering of Signature$^{TM}$ pressure gauge electronics on chassis.

attention to the highest rated model: THQR. In addition to THQR, Chapter 5 also relies on test data from the other two Signature$^{TM}$ models: TQPR and TUPR.

The THQR gauge distinguishes itself from the other Signature$^{TM}$ models in that it is rated for environments with pressures and temperatures of up to 30,000 psi and 210°C, accordingly. Gauges rated to operate in those hostile conditions are considered high-pressure, high-temperature (HPHT) tools, an industry-wide recognition of regimes in excess of 10,000 psi and 150°C. A summary of the published THQR specification is provided in Table 2.

The Signature$^{TM}$ chassis and electronics are illustrated in Figure 3, though under typical circumstances, the sensor and electronics package are welded shut inside the sensor housing. In the figure, the pressure sensing bellows is located on the right (illustrated in greater detail in Figure 5), and on the left is the pressure-sealed bulkhead. The battery pack responsible for powering the gauge screws onto the bulkhead. Finally, the gauge and battery ensemble is fitted onto a Signature$^{TM}$ carrier, which can accommodate up to four gauges, mounted 90° apart, and is capable of porting the gauges to the tubing or annulus.

Table 2: Signature$^{TM}$ THQR Gauge Specification Adapted from [1]

| Specifications | |
|---|---|
| Sensor type | HPHT Quartz |
| Pressure rating | 30,000 psi |
| Overpressure rating | 31,500 psi |
| Temperature rating | 410 psi |
| Autonomy | 37 days @ 400°F |
| | 21 days @ 410°F |
| Max. data sets | 1,250,000 |
| Memory size | 4 MB |
| Memory capacity @ 1-s sample rate | 12 days |
| Outside diameter | 1.0 in |
| Makeup length | 18.9 in |
| Weight w/o battery | 3.22 lbm |
| Material | |
| Sensor | MP35N |
| Sensor housing | Inconel 718 |
| Bulkhead | Inconel 718 |
| Battery housing | MP35N |
| **Metrology** | |
| Pressure | |
| Accuracy | 0.015% of FS |
| Resolution | 0.01 psi |
| Calibration range | Atm. to 30,000 psi |
| Drift at P/T rating | <0.025 %FS/year |
| Temperature | |
| Accuracy | ±0.9 °F |
| Resolution | 0.002 °F |
| Calibration range | 95-410 °F |
| Drift | <0.2 °F/year |
| Scanning rate | 0.1 s to 20 min |

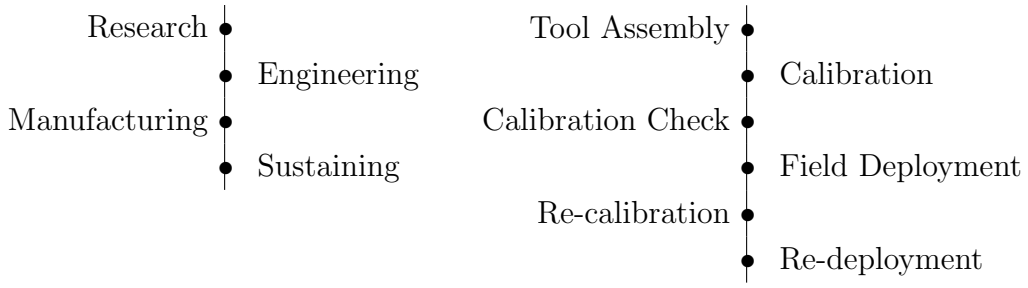


(a) Product development stages

(b) Tool lifecycle

Figure 4: Timeline of (a) the long-term stages of product development, and (b) the lifecycle of a leased pressure gauge.

### 1.2.2 Development and Use Lifecycle for a Pressure Gauge

The Research, Engineering, Manufacturing, and Sustaining (REMS) model of R&D at Schlumberger is illustrated as a long-term stage timeline in Figure 4(a). The task of optimizing gauge calibration metrology typically takes place as a subset of the Engineering efforts, though in practice it may also take place at the Sustaining stage.

More important is understanding the general gauge lifecycle illustrated in Figure 4(b). In words, once assembled, a gauge must be calibrated and checked to ensure it meets specification. This is an expensive process that can consume one week to a month at a dedicated calibration center. Gauges may be calibrated multiple times during their lifetime to guarantee specification. This costly process motivates the research in Chapter 3, which proposes subsets of THQR response surface methodologies that reduce calibration time and improve gauge accuracy.

### 1.2.3 Calibration of Pressure and Temperature Quartz Oscillators

The heart of the gauge in Figure 3 consists of three quartz oscillators, illustrated in Figure 5. Relevant to the calibration process are the pressure and temperature quartz crystals. Each crystal oscillates at natural frequency that is a function of both pressure and temperature. The temperature crystal is housed and practically isolated from most pressure changes. The pressure crystal, on the other hand, is exposed to

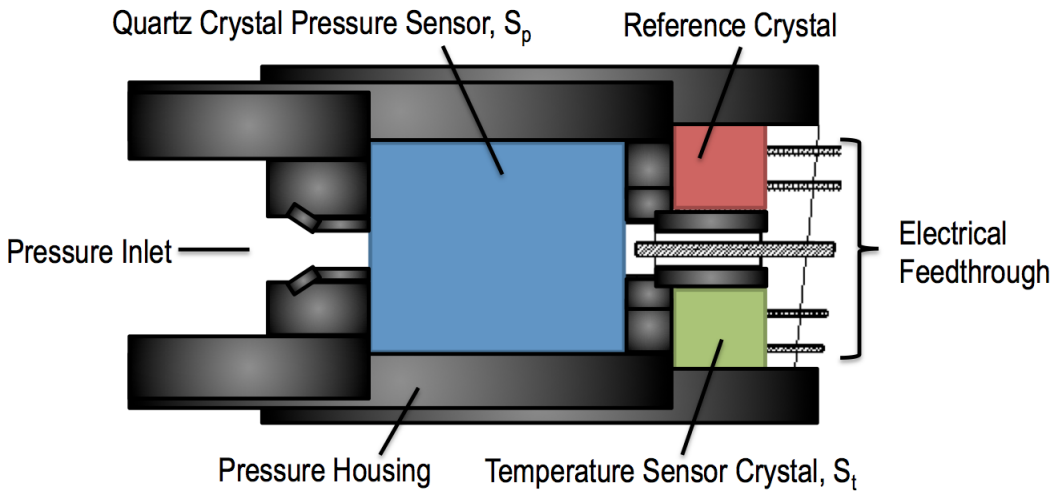


Figure 5: Pressure memory gauge with three quartz oscillators.

both pressure and temperature changes. Using a 2D polynomial, coefficients unique to each gauge define a response surface that maps static pressure and temperature crystal frequencies to useful pressure and temperatures.

Coefficients are calculated for each gauge through calibration. The coefficients are stored and used by the gauge to map quartz oscillation frequencies to useful engineering units – e.g., psi and °C. The same gauge undergoes a second calibration process known as the calibration check, where the gauge performance is verified at pressure and temperature pairs equidistant from those used in the initial calibration. Gauges that meet specification (refer to Table 2) are deployed to the field. The process is summarized in the timeline in Figure 4(b), and is detailed in Chapters 2 and 3.

## *1.3 A Final Note*

The introduction so far has provided a general context to the body of work. It should be noted, however, that this monograph tackles four fairly independent problems. For this reason, and motivated by self-sufficient compartmentalization, each chapter details introductory material that is relevant to the problem therein presented.

# CHAPTER II

# TIGHTENING THE CONFIDENCE INTERVAL ON PRESSURE-READING ACCURACY OF QUARTZ MEMORY GAUGES

The oil industry develops and improves its pressure gauges with three main metrics in mind: miniaturization, accuracy, and robustness. In well testing, much like consumer electronics markets, smaller device footprint is an attractive feature – it facilitates operator tool handling, creates space for other tools, and from a marketing standpoint, is a metric of innovation. Functionally, the tools must be rated to meet specifications that are as demanding as $\pm$ 1 psi in environments of 15,000+ psi, the equivalent of a pressure sensing resolution of a single toothpick at atmospheric pressure. And to complicate matters, modern pressure gauges are expected to meet these criteria in wells that reach exceedingly hostile pressure, temperature, and vibrational turbulences.

Oil exploration is only getting more aggressive with time, requiring a push toward more accurate well characterization of hotter and deeper wells. Thus, the motivation of this chapter is to revisit the metrology used to characterize the accuracy of high-pressure, high-temperature (HPHT) quartz memory gauges. In the process, the material seeks to familiarize the reader with the response surface methodology used to calibrate pressure gauges and their typical measurement campaign in a well flow test.

## *2.1 Introduction*

Well testing in hydrocarbon exploration heavily relies on the accuracy of pressure gauges that must perform at temperatures and pressures in excess of 300°F and 10,000 psi – a regime recognized by the oil industry as HPHT conditions. In addition to the HPHT regime, gauges must be accurate over a wide set of conditions, principally during a drill stem test (DST) for well test interpretation, but also in other applications such as gradient surveys, seabed monitoring, and fracturing jobs. A DST is a classical application where gauges are placed near inherently turbulent zones, exacerbating measurement errors and risking tool failure. Even with these challenges, pressure readings are among the most important in reservoir characterization and play an integral role in the interpretation of parameters such as productive capacity, permeability, well or formation damage, and overall commercial viability of a reservoir. The indispensable use of pressure data in well testing motivates continued improvement in their accuracy and reliability.

Gauge accuracy depends on the calibration methodology. One typical approach used for pressure gauge calibration consists of steady-state pressure and temperature combinations over which the gauge outputs are measured. Calibration polynomial coefficients map these signals (e.g., frequencies or voltages) into pressure in engineering units (e.g., psi or Pa) and a temperature correction. However, because of steady-state calibration limitations, substantial attention has been given over the last five decades to the improvement and compensation of pressure measurements through methods such as transfer functions for short- and long-term drift characterization, temperature transient compensation, and alternative dynamic calibrations [8, 14, 31, 36]. Unfortunately, these methods require a considerable logistical and economic effort because implementing a new set of compensation algorithms or calibration coefficients can present a large undertaking for both the supplier and customer. The pitfalls and proposed compensations for gauge performance are well documented, including the

gamut of electromechanical drift phenomena, adiabatic effects, and tool aging [21]. A more cost-effective alternative and practical area for improvement in gauge performance continues to be in the area of calibration methodology.

In this chapter, a study of the inherent method used in existing steady-state calibration provides new insight to the expected performance between two or more quartz memory gauges that have been calibrated using a constant and repeatable process. By comparing calibration error between pairs of gauges with unpaired sample t-tests from individual gauges, a significantly reduced variance in steady-state measurement performance can be estimated. Variance confidence intervals ($CI$) are calculated from calibration and calibration check data, a relation is developed between $CI$ estimate and gauge calibration mean quadratic deviation ($MQD$), and the results are tested against five stable pressure segments from fields in the North Sea and India.

## *2.2 Response Surface Methodology in Static Quartz Memory Gauge Calibration*

A quartz memory gauge typically consists of three quartz-oscillator sensors: the first sensor being exposed to both pressure and temperature, a second sensor to temperature only, and the clock, with a reference resonant frequency exposed but operationally immune to temperature. The frequency response of all three quartz sensors is a function of the pressure and temperature. For the purposes of this topic, only the first two quartz sensors are relevant. Additional details on quartz growth, operation, and integration are described in [22, 31].

The first quartz sensor, or pressure quartz, measures pressure changes; however, it has a nonlinear response that is also a function of temperature. The second quartz sensor, or temperature quartz, which is isolated from pressure changes, is used to correct the static thermal effects on the pressure quartz. In certain cases, the converse is true; i.e., the pressure quartz is used to compensate the temperature quartz. A quartz gauge is therefore calibrated by exposing the tool to pairs of static pressure and

temperature, and reading the output frequency from each quartz sensor. A 1D or 2D polynomial (Eq. 1) is regressed on the temperature data to calibrate the temperature quartz; another 2D polynomial (Eq. 2) is regressed on $n$ pressure/temperature pairs to produce a least-squares fit surface on the real pressure. In [31], Schultz and Chen represent these calibration polynomials as

$$T_c(n) = \sum_{i=0}^{N} \sum_{j=0}^{M} \alpha_{i,j} \left[S_p(n)\right]^i \left[S_t(n)\right]^j \tag{1}$$

$$P_c(n) = \sum_{i=0}^{N} \sum_{j=0}^{M} \beta_{i,j} \left[S_p(n)\right]^i \left[S_t(n)\right]^j \tag{2}$$

In Eqs. 1 and 2, $S_p(n)$ and $S_t(n)$ are the pressure and temperature quartz frequencies, correspondingly, and the polynomial coefficients, $\alpha_{i,j}$ and $\beta_{i,j}$, are calculated to produce least-square-fit approximations to the experimental pressure/temperature pairs, $P_e(n)$ and $T_e(n)$. The summation indices, M and N, set the polynomial order and typically range from 2 to 5; the order is a function of quartz nonlinearities, sensitivity to temperature, and desired limits on calibration error (see Eq. 3). Of particular interest in this discussion is the computed pressure approximation, $P_c$, which is used to calculate the post-calibration error, $Err(n)$, at each experimental point, $P_e$:

$$Err(n) = P_c(n) - P_e(n) \tag{3}$$

Equation 3 is subsequently used to calculate the mean squared error, or as it is known in gauge calibration, the mean quadratic deviation, ($MQD$):

$$MQD = \sqrt{\frac{\sum_{i=1}^{n} Err(n)^2}{n}} \tag{4}$$

The polynomial coefficients are expected to minimize the error, $Err(n)$, at the pressure/temperature points used to calibrate the gauge (gray squares in Figure 6). Therefore, a more realistic validation of the calibration coefficients tests the gauge

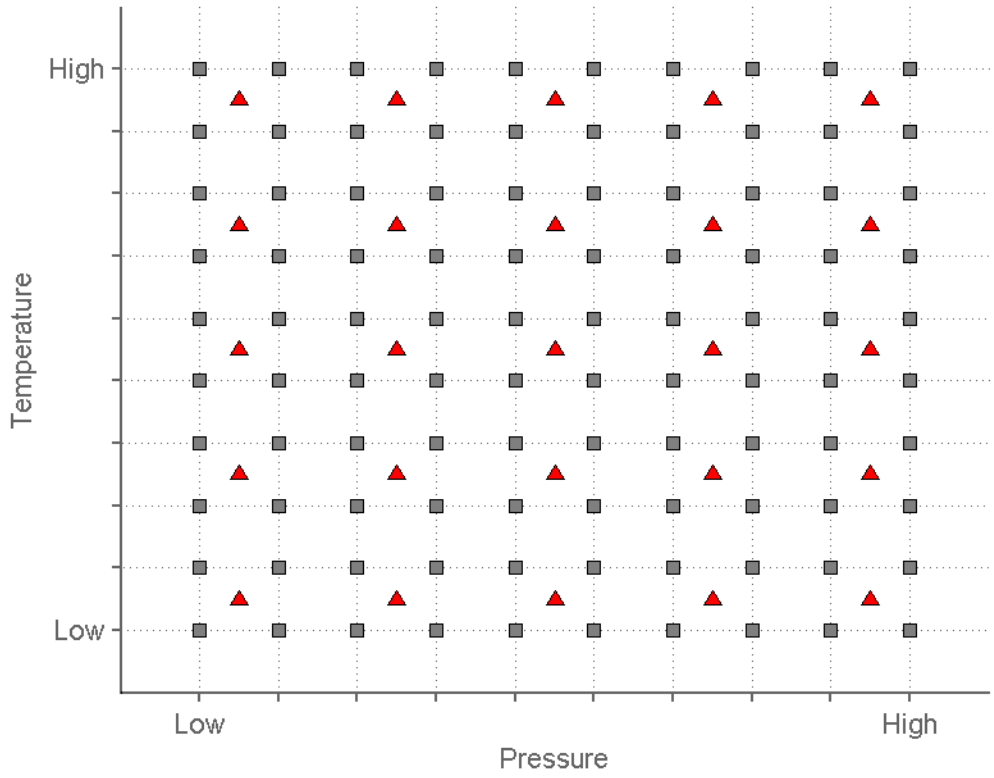


Figure 6: Pressure/temperature calibration pairs represented by squares; calibration check pairs represented by triangles.

with pressure/temperature pairs that are different from the calibration points. These new pressure/temperature points at which gauges are checked after being calibrated are called calibration check points (red triangles in Figure 6), and the temperatures and pressures computed at the calibration check points using the coefficients from the original calibration are referred to as "check data."

## *2.3 Calibration Check, Check Data, and Gauge Accuracy*

Once a calibration has been performed on a particular gauge, the polynomial coefficients are either stored in its on-board memory or used in post-processing to convert the pressure and temperature quartz frequencies to an apparent pressure (e.g., in psi).

To validate the repeatability of the measurements and the performance of the

calibration coefficients, the gauge is then tested or checked at static pressure/temperature pairs that are equidistant from the original calibration point mesh – i.e., in Figure 6 the calibration check points (red triangles) are the farthest possible distance from the calibration points (gray squares). For the least-squares fit of a polynomial surface of relatively low-order (i.e., $M, N \leq 5$), these points provide the poorest estimate in performance or the largest error over the tool's rated operating range (Eq. 3). Figure 6 illustrates the selection of the calibration check points relative to the regular calibration points.

Using the results from the calibration and the calibration check, gauge accuracy is calculated and validated. The current HPHT quartz memory gauge has an accuracy specification of $\pm 7.5$ psi. This accuracy specification is a function of the dead weight tester (DWT) accuracy, the gauge accuracy, and the full-scale (FS) pressure[1].

## *2.4 Measurements of Measurands Produced by Two Stable Processes*

In previous work, Kabir and Pop [19] used the Student t-test to calculate the accuracy of compositional gradients of gas-condensate reservoirs. Jackson et al. [17] and Zhou et al. [37] used a comparable method to determine if subtle pressure gradient differences are statistical or real. From a calibration standpoint, a similar method is proposed to provide confidence limits between gauges using the two-sample or unpaired sample t-test.

The application of the unpaired sample t-test to the aforementioned calibration method provides limits for the difference in the process mean of the measurands: the gauge error per calibration point or check point. Simply, the t-test provides a confidence interval ($CI$) on the variance in the error difference between two gauges

[1] Gauge Accuracy = Dead Weight Tester Accuracy + Gauge-Inherent Accuracy
= 0.01% · FS + 0.015% ·FS;
HPHT Quartz Memory Gauge FS = 30,000 psi

that have been calibrated using the same process. Most simply, the t-test helps determine to a confidence level (for instance, 99.9% confidence) the interval that contains the difference between two sets of measurements. In the context of gauges, the confidence interval sets the bounds that would contain the difference in the error between the two calibrated gauges.

The t-test is one type of hypothesis test, and is comparable to the z hypothesis test, which is generally preferable when dealing with large measurement sets (typically when $n > 30$). However, the t-test is preferable when the standard deviation is not known and the z-test requirements cannot be guaranteed. Regardless, for sufficiently large data sets, the t-test procedure begins to behave nearly identically to the z-test.

The most attractive feature of the two sample t-test is that it can be leveraged to remove the bias in a process, a detail which motivates the use of the same in the rest of this chapter and is discussed in greater detail through the end of this section, culminating in Eq. 9. In short, the test provides a method of estimating the difference in error between calibrated gauges with the methodic exclusion of any systematic and linear bias in the calibration process, a method that Vardeman et al. discuss at great length in [33–35].

This unpaired sample t-test assumes that the calibration process is constant (e.g., the technician follows a consistent procedure) and that the calibration device is linear (i.e., the bias is constant). These conditions are often met in industrial-grade calibration setups: a DWT and a temperature-generating system with accuracies of approximately 0.01% and 32.2°F of FS reading, respectively. The calibration process also has inherent bias ($\delta$) and variance ($\sigma^2_{device}$) that are additive to the gauge bias ($\mu_G$) and variance ($\sigma^2_G$). The calibration bias can be computationally eliminated by taking the difference of the calibration errors of two gauges [35]. Figure 7 shows how two gauges are each calibrated or, alternatively, checked post-calibration, at $n$ pressure-temperature pairs.

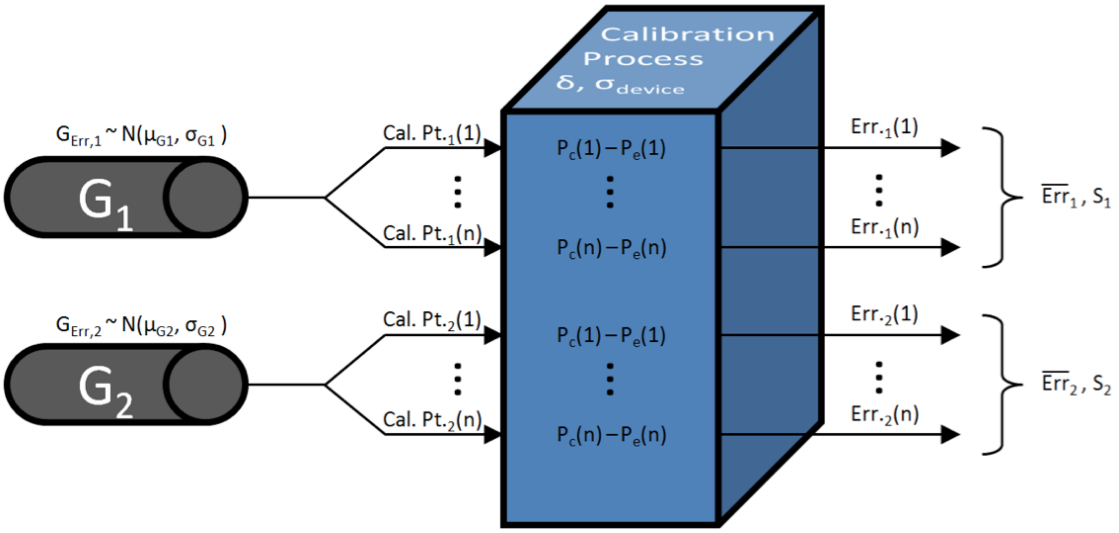


Figure 7: Single measurements using the calibration device on two independent pressure gauges.

For any two gauges, their respective calibration errors, $Err_1$ and $Err_2$, are normally distributed and independent of each other, such that

$$Err_1 \sim N\left(\mu_{G1} + \delta, \sqrt{\sigma_{G1}^2 + \sigma_{device}^2 + 2\sigma_{G1,device}}\right) \tag{5}$$

$$Err_2 \sim N\left(\mu_{G2} + \delta, \sqrt{\sigma_{G2}^2 + \sigma_{device}^2 + 2\sigma_{G2,device}}\right) \tag{6}$$

where the gauges and devices are uncorrelated, covariance of the gauges and device ($\sigma_{G,device}$) are near-zero relative to the gauge and device variances, and the gauge variance will typically be greater than that of the device.

The Lilliefors normality test, an adaptation of the Kolmogorov-Smirnov test for data with unknown mean and variance, was used to test the null hypothesis that the collective errors in calibration and calibration check data come from a normally distributed population. The test validated to a 95% confidence level the uniformity assumptions of the error distributions [23]. A visualization of the error distribution is included in Appendix A.1.

The errors in Eqs. 5 and 6 can be estimated by calculating the mean error ($\overline{Err}_1$

and $\overline{Err}_2$) and standard deviation ($S_1$ and $S_2$) of each gauge. Given that the device is linear and the calibration errors are uniform and independent, the $\hat{t}$ confidence interval that compares the difference in error between $n_1$ and $n_2$ samples of gauges $G_1$ and $G_2$, respectively, is

$$CI = \overline{Err}_1 - \overline{Err}_2 \pm \hat{t}\sqrt{\frac{S_1^2}{n_1} + \frac{S_2^2}{n_2}} \tag{7}$$

where the $\hat{t}$ "approximate degrees of freedom," $\hat{\nu}$, are defined by

$$\hat{\nu} = \frac{\left[\frac{S_1^2}{n_1} + \frac{S_2^2}{n_2}\right]^2}{\frac{S_1^4}{(n_1-1)n_1^2} + \frac{S_2^4}{(n_2-1)n_2^2}} \tag{8}$$

The main implication of Eq. 7, vis-à-vis gauge specification, is that the unpaired sample Satterthwaite approximate $\hat{t}$ interval provides limits for the difference in the measurands – in this case, the error between two pressure gauges – and in the process, removes the device bias from the calculation:

$$(\mu_{G1} + \delta) - (\mu_{G2} + \delta) = \mu_{G1} - \mu_{G2} \tag{9}$$

## *2.5 A Note on the Paired Sample t-Test*

The unpaired sample t-test assumes uncorrelated gauge error sets. However, preliminary tests show gauge correlation values $\geq 0.9$ for calibration data and $\geq 0.6$ for gauge-check data, evidence that the errors between gauges at identical depth are significantly correlated. This correlation is likely due to similarities in the coefficient matrices produced in the calibration of each gauge.

Given this correlation, this is a good place to introduce the paired sample t-test. In contrast to the unpaired sample t-test, the paired t-test offers a more powerful statistic. Specifically, the error term in Eq. 7 could be replaced with the estimated standard error of the difference between correlated sample means:

$$\sqrt{\frac{S_1^2}{n_1}+\frac{S_2^2}{n_2}} \rightarrow \sqrt{\frac{S_1^2}{n_1}+\frac{S_2^2}{n_2}-\frac{2r_{12}S_1S_2}{\sqrt{n_1n_2}}} \;\; \forall \;\; r_{12} = \text{correlation term} \tag{10}$$

Thereby, Eq. 7 becomes

$$CI = \overline{Err}_1 - \overline{Err}_2 \pm \hat{t}\sqrt{\frac{S_1^2}{n_1}+\frac{S_2^2}{n_2}-\frac{2r_{12}S_1S_2}{\sqrt{n_1n_2}}} \tag{11}$$

The effect of the covariance term in Eq. 10 clearly reduces the $CI$ because correlation between calibrated gauges is typically strictly positive. The remainder of the chapter, however, will continue to focus on the unpaired sample t-test, and the analysis is therefore expected to conservatively estimate the $CI$ in error between gauges.

## *2.6 Error in Calibration and Calibration Check Readings*

The difference in error reading between 31 pressure gauges using calibration data is within 1.2 psi with a confidence of 99.9%. The mean difference across all gauges is relatively small, centered about zero and rarely exceeds 0.06 psi. Figure 8 provides a complete picture of the mean difference and confidence ranges for the set of gauges using only the calibration data.

The calibration data are expected to give a much tighter and optimistic $CI$ than the check data. Nonetheless, Figure 8 gives some inference on the broadening factor going from best-case to worst-case performance. Figure 9 provides the $CI$ statistics on check data between 10 gauges, which are more conservative and realistic statistics. For gauge-check data, the mean-difference error is 0.096 $\pm$0.47 psi and the $CI$ spread is centered at 2.13 $\pm$0.33 psi.

The check data statistics show that the mean-difference error is greater than the estimated error in calibration data by an order of magnitude. A second observation is that the $CI$ range nearly doubles across all gauges. This degradation in check data performance is not unexpected; the degree of degradation is a useful parameter

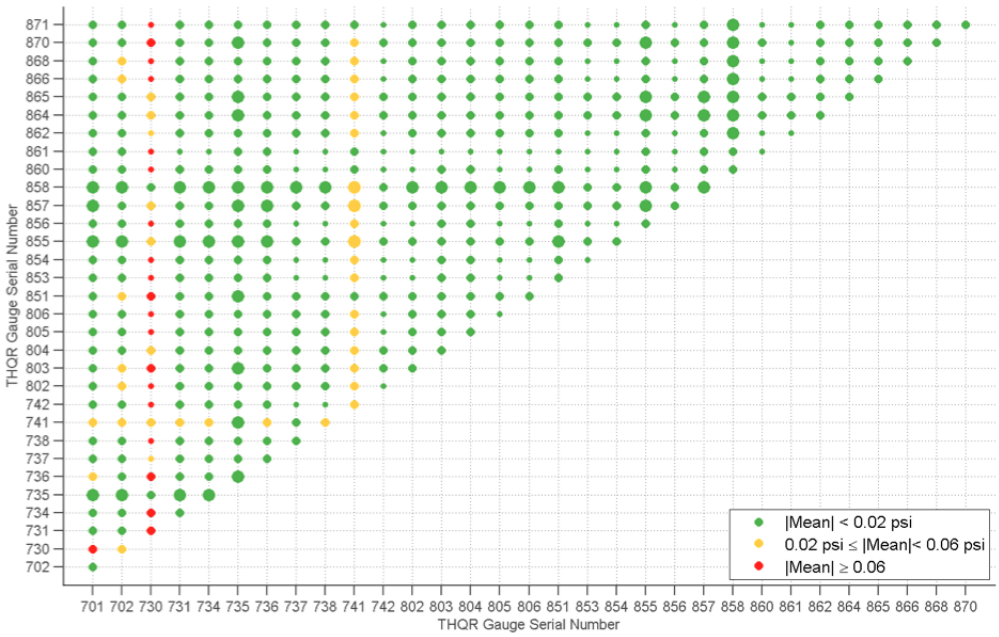


Figure 8: Scattering of confidence interval ($CI$) ranges in the error difference for any two of 31 quartz memory gauges using calibration data. The size of the marker is proportional to the $CI$ magnitude; i.e., small for $CI < 1.1$ psi, medium for 1.1 psi $\leq CI < 1.3$ psi, and large for $CI \geq 1.3$ psi.

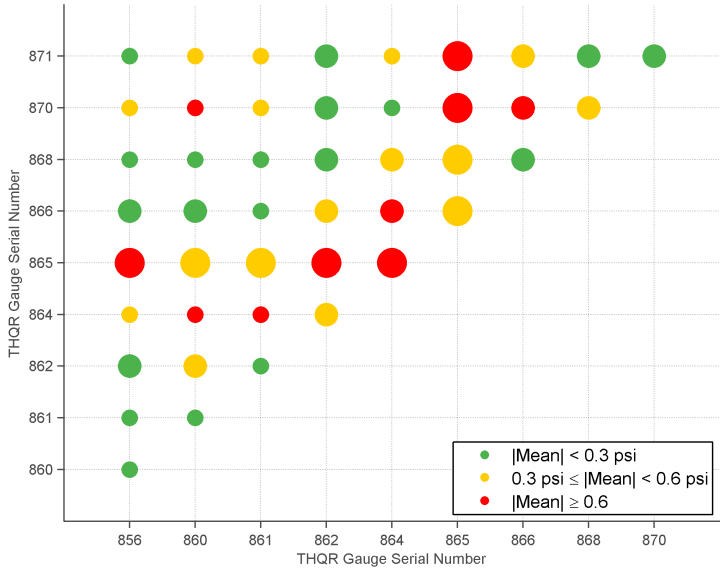


Figure 9: Scattering of confidence interval ($CI$) ranges in the error difference for any two of 10 quartz memory gauges using calibration check data. The size of the marker is proportional to the $CI$ magnitude; i.e., small for $CI < 2.0$ psi, medium for 2.0 psi $\leq CI < 2.4$ psi, and large for $CI \geq 2.4$ psi.

to calculate the broadening factor between the $CI$ estimated by the Satterthwaite interval (Eq. 7) and the empirical $CI$ in the error of two gauges in a well.

## *2.7 Calibration Effects on CI for the Mean-Difference Error between Two Gauges*

The $\hat{t}$ confidence interval in Eq. 7 produces a mean-difference error, a $CI$, and a $CI$ range (see Eq. 12a). However, in HPHT gauges, the $CI$ range for both calibration- and gauge-check data is greater than the mean-difference error, as the latter tends to be small. In short, there are several reasons why the $CI$ range is a metric of greater value than the mean-difference error:

- The mean-difference error measurement between two gauges is typically small and near zero.
- The $CI$ range is 4 to 10 times greater than the mean-difference error.
- The $CI$ capably quantifies the pressure measurements between gauges to a 99.9% confidence level.

The difference of the $CI$ bounds – presented in Eq. 7 as an upper and lower bound (i.e., the $\pm$ term) – is proportional to the product of the $\hat{t}$ confidence interval and the root term:

$$CI_{Range} = CI_{upper} - CI_{lower} = 2\hat{t}\sqrt{\frac{S_1^2}{n_1} + \frac{S_2^2}{n_2}} \tag{12a}$$

Let $\mathbf{X}$ and $\mathbf{Y}$ be the random calibration errors of Gauge 1 and Gauge 2, respectively. Substituting the biased sample variance in Eq. 12a yields

$$CI_{Range} = 2\hat{t}\sqrt{\frac{\frac{1}{n_1}\sum_{i=1}^{n_1}(x_i - \overline{x})^2}{n_1} + \frac{\frac{1}{n_2}\sum_{j}^{n_2}(y_j - \overline{y})^2}{n_2}} \tag{12b}$$

where, for the case of Gauge 1, $n_1$ is the number of error samples, $x_i$ is a sample, and $\overline{x}$ is the sample mean. The respective parameters for Gauge 2 are $n_2$, $y_j$, and $\overline{y}$.

Keep in mind that $\mathbf{X}$ and $\mathbf{Y}$ are normally distributed, and near zero-mean random variables. In addition, gauges are typically tested at the same number of points. With these simplifications, the $CI$ range reduces to

$$CI_{Range} = \frac{2\hat{t}}{n}\sqrt{\sum_{i=1}^{n} x_i^2 + \sum_{j=1}^{n} y_j^2} \;\; \forall \; n = n_1 \cong n_2 \tag{12c}$$

To provide Eq. 12c with some context, it is useful to revisit the metrology behind individual gauge calibrations. To match notation, the $MQD$ that was introduced in Eq. 4, and which is a useful metric of calibration quality, is rewritten as

$$MQD_x = \sqrt{\frac{\sum_{i=1}^{n} x_i^2}{n}} \tag{13a}$$

and the summation is isolated to match each summation term in Eq. 12c:

$$\sum_{i=1}^{n} x_i^2 = n \cdot MQD_x^2 \tag{13b}$$

Substituting Eq. 13b into the $CI$ range approximation (Eq. 12c) yields

$$CI_{Range} = \frac{2\hat{t}}{\sqrt{n}}\sqrt{MQD_x^2 + MQD_y^2} \tag{14}$$

where each subscript denotes a unique gauge.

Thus, the range of the $CI$ is directly proportional to the sum of the square, or 2-norm, of the $MQD$s of two pressure gauges. A conservative approximation to guarantee to 99.9% significance that the error in the difference between two gauges will be within ±2 psi (i.e., a $CI$ range of 4 psi) is that their $MQD$ norm be less than 2.2 psi. This limit in mean-difference error between gauges excludes the calibration tool accuracy; in the instance of a DWT with 0.01% accuracy at FS of 30k psi (i.e., ±3 psi), the upper and lower bounds on tool and calibration errors combined for any given gauge is unlikely to exceed ±5 psi.

Note that any gauge with a large $MQD$ will dominate the limit on $CI$. Compensating a large $MQD$ gauge with a low $MQD$ gauge may prove difficult if the disparity

is sufficiently large; i.e., the square of the larger $MQD$ will dominate, especially in the case where a more accurate gauge has $MQD < 1$ (refer to Eq. 14).

## *2.8 Case Study: Simultaneous Gauge Performance on Stable Pressure Regimes*

Five DST runs under stable pressure regimes (e.g., soon after shut-in during a buildup) from the North Sea and India regions were analyzed to verify if simultaneous gauge measurements agreed with the limits derived from the Satterthwaite $CI$ (Eq. 14). Figure 10 provides typical DST pressure and temperature events and highlights a stable pressure regime (shown in yellow) after shut-in.

Each segment had two or more gauges at identical tool height; their pressure recordings were used to calculate the disparity across stable conditions between all possible combinations of paired gauges. The five segments belonged to HPHT well tests: North Sea "A", North Sea "B", North Sea "C", India "A", and India "B". Table 3 summarizes the number of gauges used on each segment, their respective calibration batch, and their calibration accuracy ($MQD$).

The third column in Table 3, unique calibration batches, deserves special attention. Gauges are often calibrated in batches and then deployed in unison to the field. It is not rare, however, to use gauges from different calibration batches in the same well. For instance, North Sea "A" has four gauges, two from one calibration batch (denoted by a bold **A**) and the other two from a different batch (denoted by a bold **B**). Initially, gauges from the same calibration batch were expected to have tighter $CI$ in pressure readings than gauges from different batches. This batch criterion relates to the statistical method's requirement for an identical calibration process. Results, however, confirm that gauges have comparable $CI$ in readings, independent of calibration batch. These results suggest that the method and process used to calibrate the quartz gauges is highly constant, stable, and repeatable.

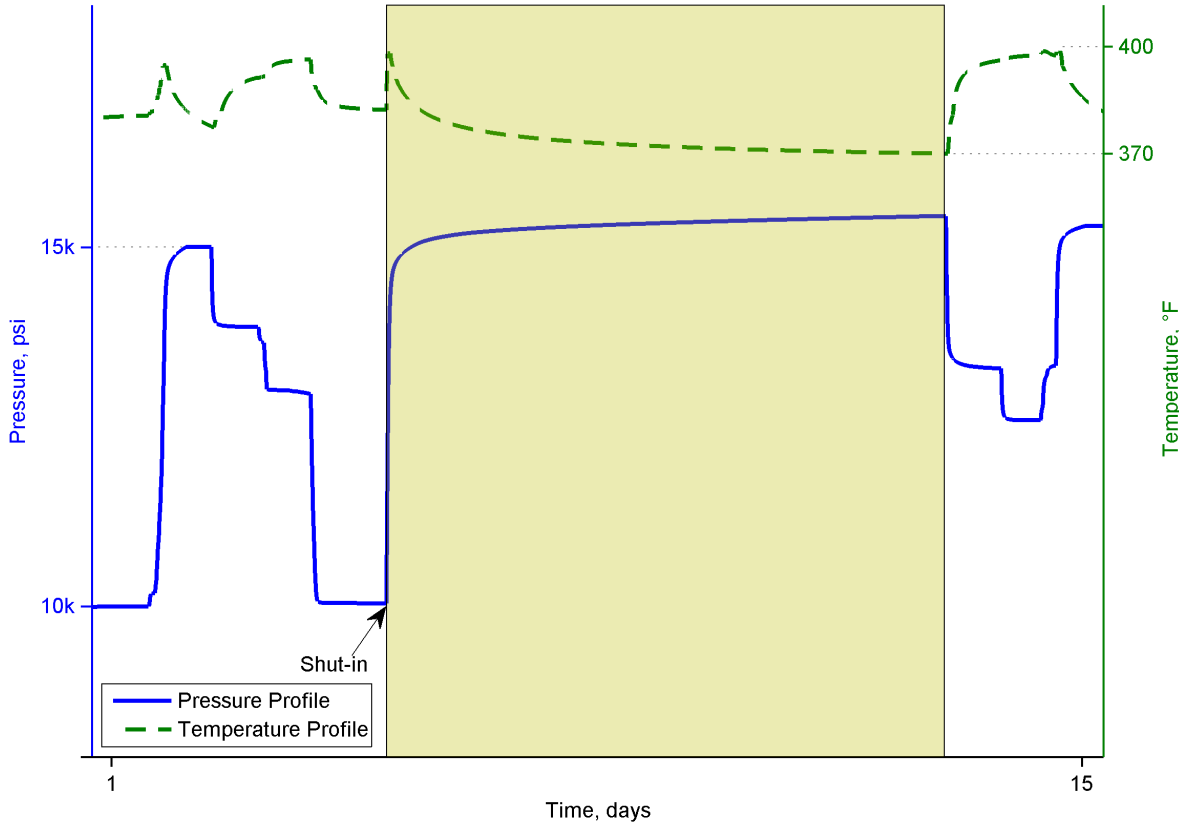


Figure 10: Example of downhole pressure and temperature profiles recorded by a quartz gauge. The yellow segment highlights the segment of interest: a pressure buildup and subsequent stabilization. Scales are indicated.

Table 3: Gauges, Calibration Sets, and $MQD$ for Stable Field Segments

* Gauges with the same bold letter were calibrated on the same date, and belong to the same calibration batch.

| Stable Field Segment | Gauges in Well | Unique Calibration Batches | Calibration Accuracy ($MQD$) |
|---|---|---|---|
| North Sea "A" | 4 | **A** | 1.372 |
| | | **A** | 1.492 |
| | | **B** | 1.220 |
| | | **B** | 1.315 |
| North Sea "B" | 2 | **A** | 1.372 |
| | | **A** | 1.492 |
| | | **B** | 1.220 |
| | | **B** | 1.315 |
| North Sea "C" | 2 | **A** | 1.072 |
| | | **A** | 1.492 |
| India "A" | 3 | **C** | 1.211 |
| | | **C** | 1.053 |
| | | **D** | 1.200 |
| India "B" | 3 | **C** | 1.048 |
| | | **C** | 0.968 |
| | | **D** | 1.200 |

## 2.9 Pressure Difference Performance across All Gauges

For each segment and tool with $n$ simultaneous gauges, there were $\binom{n}{2}$ combinations of unique pressures differences. These pressure differences are indicated in Figure 11 by solid lines with the pressure profile of their corresponding segment as a black dotted line. On each segment the time axis has been normalized to the DST's shut-in event. The respective mean pressure difference and standard deviations of each interval containing 99.9% of pressure difference points for each segment are summarized in Table 4.

## 2.10 Quartz Gauge Performance in the Field

All of the field gauges in this series of tests met the predicted maximal difference in pressure measurement at stable regimes. Table 4 summarizes the performance for each gauge; the last row shows the mean difference in pressure measurements calculated per segment, so that 99.9% of the pressure differences are contained within that range. For example, on the average, 99.9% of the pressure differences between all gauge pairs in the North Sea "A" segment are contained between $-0.44$ psi and 0.20 psi. No gauge pair exceeds the difference limit of $\pm 2$ psi, validating the proposed relationship between the $MQD$ norm and the $CI$ (Eq. 14).

The inverse problem also validates the relationship between $MQD$ norm and $CI$. Considering the widest range in pressure difference across all HPHT segments (refer to the last row of Table 4) as the worst-case scenario, a $CI$ of 1.82 psi (corresponding to the limits $-0.44$ to 1.38 psi) requires an $MQD$ norm less than or equal to 1.997 psi (found by solving for the radical in Eq. 14). Values used for the calculation of Eq. 14 are an average of the sample counts in calibration and check measurements, $n = (91 + 24)/2$, and an average of the $\hat{t}CI$ for the average degrees of freedom, $\hat{t} = (3.36 + 3.55)/2$, where degrees of freedom are typically around 150 for the calibration and 40 for the calibration check (using Eq. 8). The degrees of freedom are given by

Table 4: Mean pressure difference ($|\mu|$ psi) and standard deviations ($\sigma$ psi) for each segment.

| Gauge Pair | North Sea "A" | | | North Sea "B" | | | North Sea "C" | | | India "A" | | | India "B" | | |
|---|---|---|---|---|---|---|---|---|---|---|---|---|---|---|---|
| Identifier | $\lvert\mu\rvert$ | $\sigma$ | $\mu \pm 3.3\sigma$ | $\lvert\mu\rvert$ | $\sigma$ | $\mu \pm 3.3\sigma$ | $\lvert\mu\rvert$ | $\sigma$ | $\mu \pm 3.3\sigma$ | $\lvert\mu\rvert$ | $\sigma$ | $\mu \pm 3.3\sigma$ | $\lvert\mu\rvert$ | $\sigma$ | $\mu \pm 3.3\sigma$ |
| 1 | 0.12 | 0.07 | $[-.035, 0.12]$ | 0.09 | 0.05 | [-0.26,0.08] | 1.12 | 0.08 | [0.86,1.38] | 0.93 | 0.05 | [0.76,1.11] | 0.96 | 0.10 | [0.64,1.27] |
| 2 | 0.30 | 0.11 | $[-0.67, 0.08]$ | 0.32 | 0.09 | [-0.62,-0.02] | | | | 0.75 | 0.07 | [0.51,0.99] | 0.23 | 0.11 | [-0.13,0.59] |
| 3 | 0.19 | 0.03 | $[-0.28, -0.09]$ | 0.16 | 0.03 | [-0.26,-0.05] | | | | 0.18 | 0.03 | [-0.27,-0.09] | 0.73 | 0.02 | [-0.79,-0.67] |
| 4 | 0.18 | 0.18 | $[-0.78, 0.42]$ | 0.23 | 0.14 | [-0.69,0.24] | | | | | | | | | |
| 5 | 0.11 | 0.14 | $[-0.35, 0.57]$ | 0.17 | 0.12 | [-0.24,0.57] | | | | | | | | | |
| 6 | 0.07 | 0.04 | $[-0.22, 0.08]$ | 0.07 | 0.02 | [-0.15,0.01] | | | | | | | | | |
| Segment Mean | 0.16 | 0.10 | $[-0.44, 0.20]$ | 0.17 | 0.08 | [-0.37,0.14] | 1.12 | 0.08 | [0.86,1.38] | 0.62 | 0.05 | [0.33,0.67] | 0.64 | 0.07 | [-0.09,0.40] |

* Note: For normally distributed data,
99.9% of the points are contained within $3.2906\sigma$ of the mean.

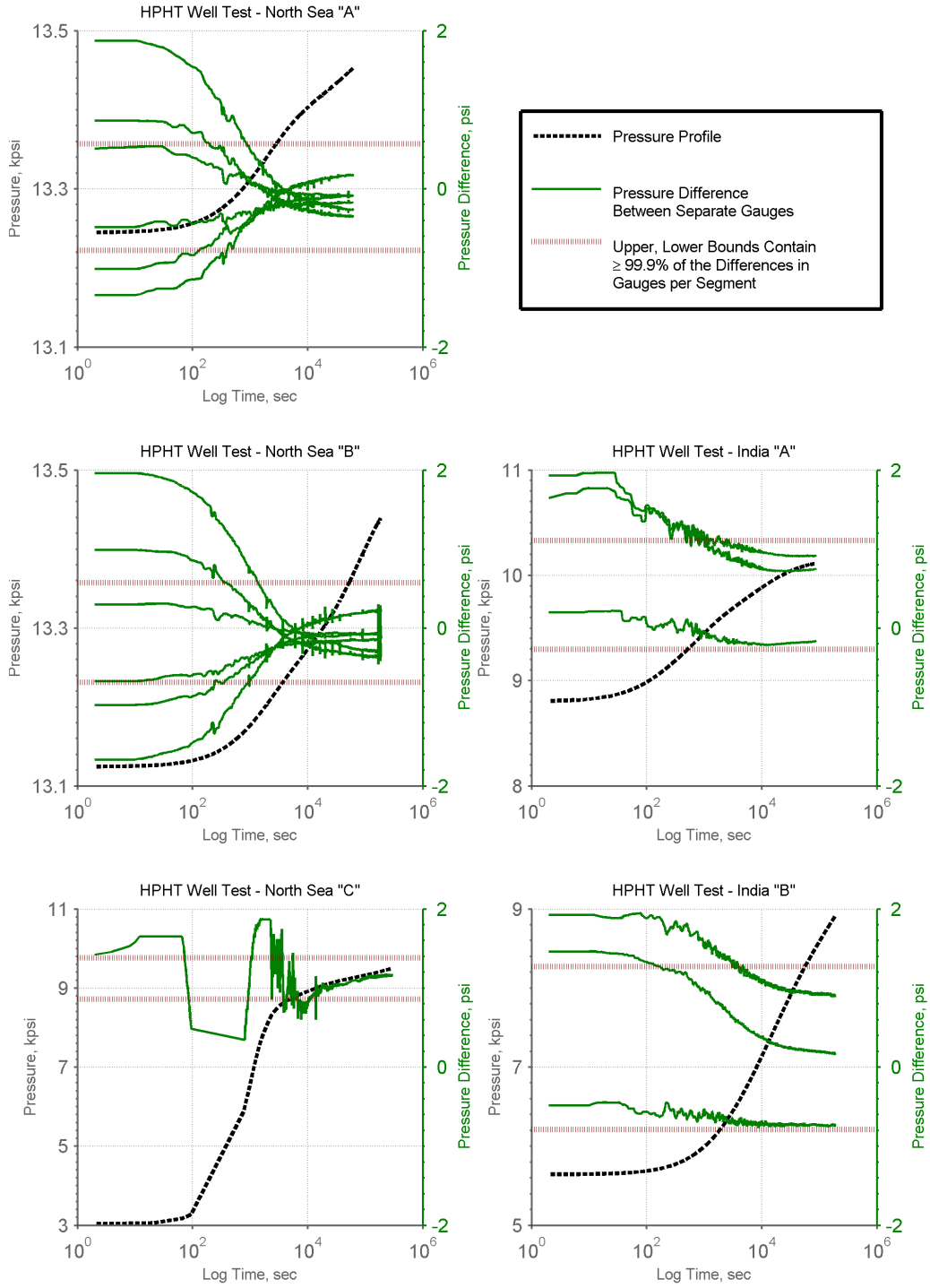


Figure 11: Pressure profiles (dotted black lines) and pressure differences between gauges (solid green lines) on five HPHT well tests. Upper and lower bounds (dotted red lines) contain $> 99.9\%$ of the pressure differences for all the gauges in the segment.

* Note: Each DST profile was time-normalized to the shut-in event.

the number of samples and consequently, of values that are free to vary in a statistic. The Satterthwaite approximation yields effective degrees of freedom for unpaired sample sets and takes into account the number of samples and the variance in each set (Eq. 8). The large number of check data points and larger number of calibration points account for the given degrees of freedom.

Of all the HPHT gauges in the study, the highest $MQD$ norm is equal to 2.03 psi, which is 0.17 psi less than the suggested $MQD$ norm limit.

## *2.11 Finding the Stable Regime*

So far, the concept of "stable pressure regime" has been used freely and without quantitative metric. While it is beyond the scope of this chapter to define a general metric for the stable regime, calculating the rate of pressure change at which the gauges begin to perform in a stable manner helps to give a notion of the onset of stability. As the projected $CI$ for pressure difference between any of the HPHT gauges was calculated to be $\pm 2$ psi, a possible definition of the stable regime is the time at which the difference between all gauge readings falls under the $\pm 2$ psi limit. Figure 12 shows the rate in pressure change for each segment at the point after shut-in when all gauges are reading within 2 psi of each other. Table 5 includes the time elapsed between shut-in and the onset of stability, as well as the mean rate of pressure change for the first 10 sec of stability. It must be noted that the onset of stability is reservoir dependent; e.g., a highly permeable reservoir with good pressure support may stabilize almost instantly. For the HPHT reservoirs in the case study, the accuracy statements are valid on the average as early as 17.4 min after shut-in.

The method for estimating the disparity between multiple gauges at the onset of stability raises some important questions. First, the sampling clocks between gauges are unlikely to be running synchronously, partly due to the time offset if the switch from passive to active measurement mode is inexact, and partly due to

the difference in clock drifts (a variable mechanism related to circuit temperature). Therefore, alignment between two pressure signals is necessary and can be achieved by shifting one signal until the correlation between both signals is maximized. Time drift in both gauges is expected to be comparable, as they are going to witness the same temperature changes. In addition, signal sample times need to be synchronized to calculate accurately the difference in readings. One way of achieving this is to interpolate the signal of one gauge using the clock of the secondary gauge. The current study uses linear interpolation; i.e., an approach that is simple but can produce more conservative estimates than alternatives (e.g., spline or polynomial interpolations). Therefore, while the calculation in error between the tools is expected to deteriorate due to the drift and time shifts, processing methods help mitigate these effects.

Table 5 shows that stable conditions are typically reached within the first hour of buildup. In the North Sea "C" segment, stability immediately followed shut-in; the other HPHT segments required between 5 and 33 min to reach stable conditions; i.e., gauges reach stability in less than an hour. These results mean that upwards of 95% of the measurements during buildups will meet the proposed specification of ±5 psi, useful information when considering that accuracy becomes progressively better, and more valuable, as the buildup evolves.

## *2.12 Conclusions*

The statistical measurement methodology of an unpaired sample t-test confirms existing evidence that some HPHT gauges from certain manufacturers perform far better than their published specifications. In addition, it has been shown, both through the proposed methodology and empirically through the study of five HPHT well tests, that quartz gauges outperform their specification by over 30%, an improvement from ±7.5 psi to ±5.0 psi. Detailed analysis of the standard calibration process offers insight into the relationship between a single-gauge $MQD$ and coupled gauge accuracy

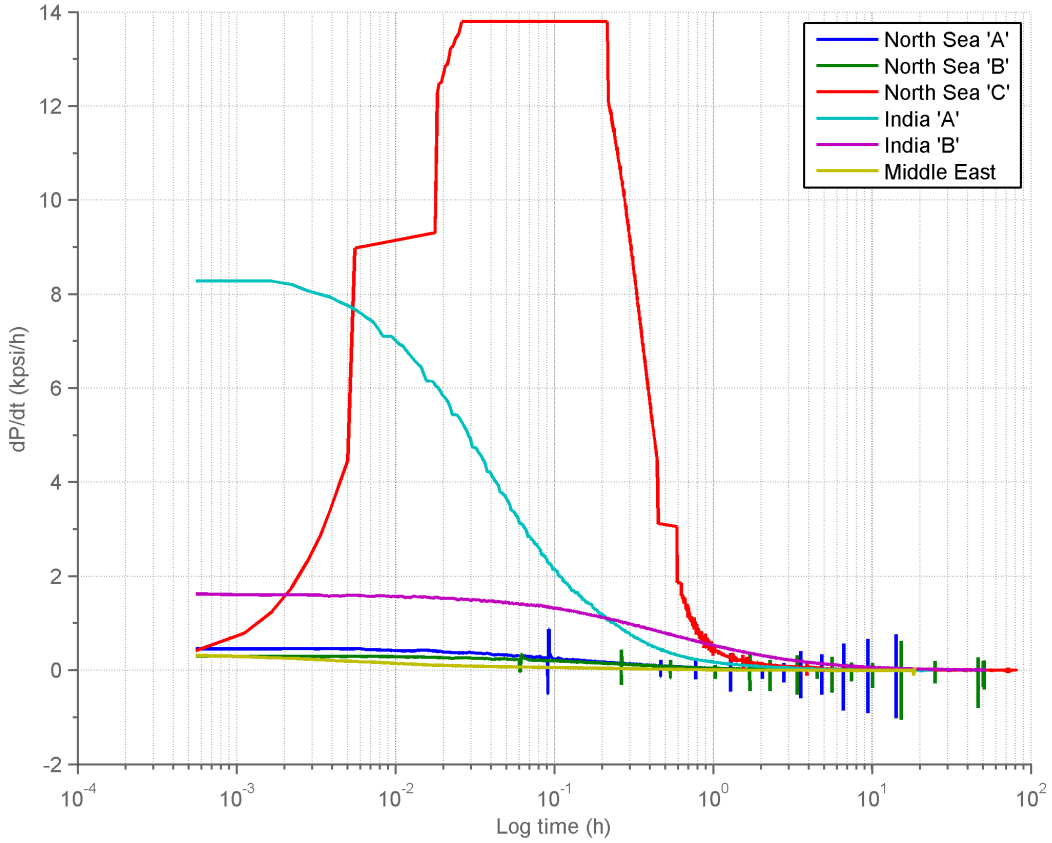


Figure 12: Rate of pressure change for all five well test segments at the onset of a stability of ±2 psi pressure difference.

Table 5: Pressure Gradient over 10 Seconds after Onset of a Stable Regime

| Segment | Shut-in to Stabilization Time (min) | Initial 10-sec dP/dt (psi/h) |
|---|---|---|
| North Sea "A" | 19.20 | 457.58 |
| North Sea "B" | 33.00 | 297.35 |
| North Sea "C" | 0.00 | 895.24 |
| India "A" | 5.40 | 8257.29 |
| India "B" | 29.34 | 1611.17 |
| AVERAGE | 17.39 | 2303.73 |

that validates current field performance. Significant findings include:

- The predicted difference in measurements between any two HPHT quartz memory gauges is to be consistently less than ±2 psi, which the requirement that their $MQD$ norm be less than 2.2 psi.
- No HPHT gauge pair from five stable segments was found to exceed the difference limit of ±2 psi.
- More than 95% of the measurements during a buildup met the specification of ±5 psi.
- Memory gauge calibration process was found to be highly constant from one batch to the next.
- The unpaired sample t-test can be applied to variations of the calibration process that meet only a few criteria: normal distribution of error, independence in errors, constant and repeatable calibration process, and linear bias of calibration devices.

The unpaired t-test methodology should not only be used in the reevaluation of existing tool specifications, but also be integrated into existing metrological standards in the oil industry where painstakingly accurate tools and calibration devices are commonly found. The methodology is particularly attractive in areas of research and manufacturing of electronics that play a leading role in exploring, interpreting, and eventually extracting hydrocarbons and other natural resources.

# CHAPTER III

# EFFECTS OF UNLIKELY DOWNHOLE CONDITIONS ON GAUGE CALIBRATION ACCURACY

Chapter 2 introduced the response surface methodology required to calibrate quartz sensor gauges. First, the mesh of pressure/temperature pairs over which gauges are calibrated was visualized in Figure 6, and the polynomial regressions that computed the quartz response at each calibration point were defined in Eqs. 1 and 2. Finally, the metric of calibration quality for a particular gauge, the mean quadratic deviation ($MQD$), was introduced in Eq. 4. This is a good place to remind the reader that the calculation of the polynomial coefficients in Eqs. 1 and 2 are selected so as to minimize $MQD$.

This chapter builds on the calibration process presented in Chapter 2 and focuses on the challenge of optimizing the pressure/temperature pairs that are included in the calibration mesh. Specifically, the chapter seeks to evaluate the effects on calibration accuracy after removing calibration pairs. Pairs removed are those that are deemed as unrealistic or unlikely downhole conditions – e.g., low pressures, or high pressures at low temperatures. This evaluation relies on existing calibration data for the Signature$^{\text{TM}}$ THQR gauge specified in Table 2.

## *3.1 Signature$^{TM}$ THQR Gauge Calibration*

The calibration and calibration check of the THQR pressure gauges requires that each unit be experimentally measured in static conditions over pressure and temperature steps that range from Atm – 30,000 psi and 35 – 210°C, accordingly. A total of 91 experimental $S_p/S_t$ couples are regressed using 2D Legendre polynomials (Eqs. 1

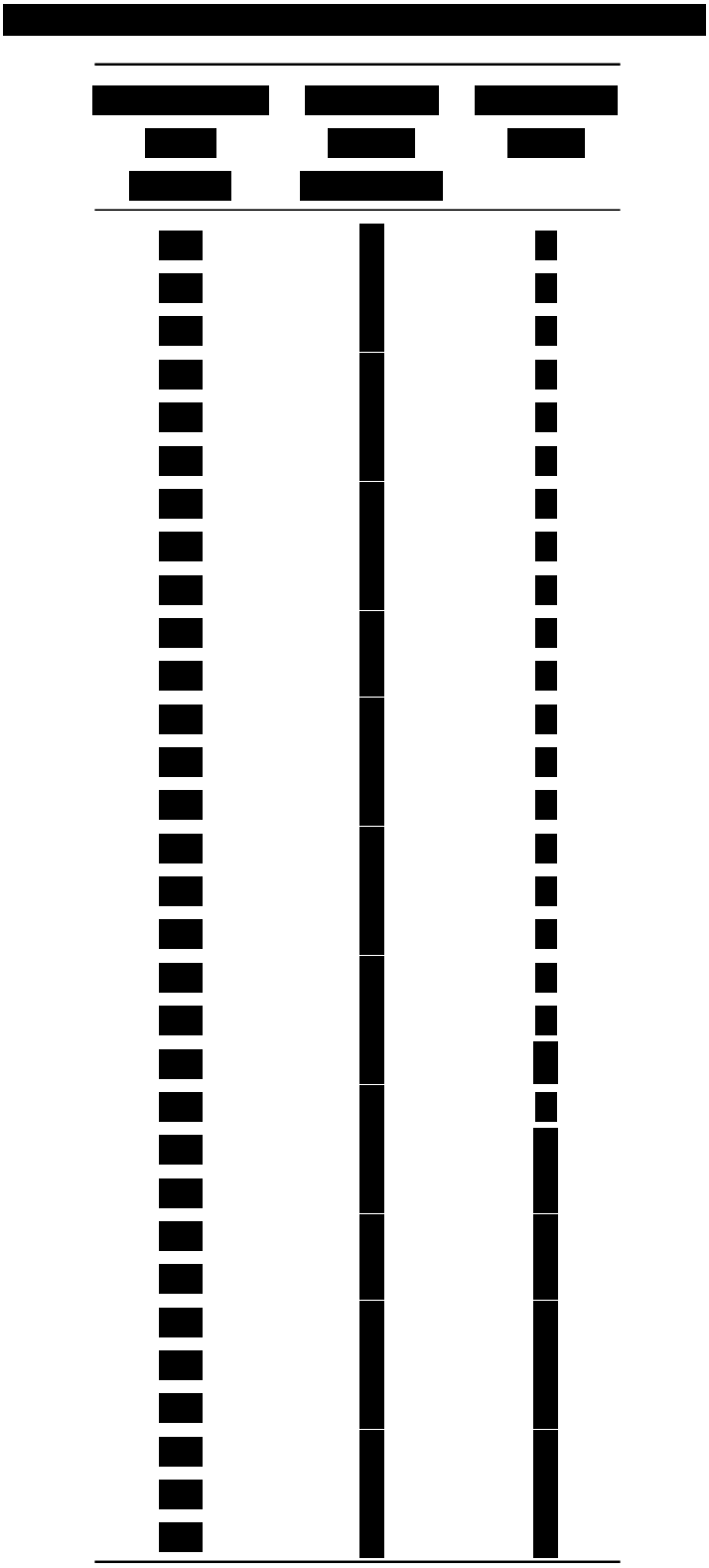

and 2) and a coefficient matrix is calculated for each gauge. Set 1 in Figure 13 provides the specific mesh of calibration pressure/temperature pairs. Sets 2–4 are explained in more detail in Section 3.2.1.

This chapter recalculates the coefficient matrices using subsets of calibration data and evaluates the metrology on 32 THQR tools. The coefficient matrices are evaluated with the calibration check measurements of 10 gauges. These commercial gauges are identical in their manufacturing and calibration process, and each is identified by a serial number. Both the calibration and calibration check gauges are identified by serial number in Table 6.

## *3.2 Method for Coefficient Matrix Evaluation*

### 3.2.1 Testbed

For each of the 32 calibration gauges, a MATLAB structure stores the gauge serial number, the frequencies recorded by the pressure quartz ($S_p$) at each calibration point, the frequencies recorded by the temperature quartz ($S_t$) at each calibration points, and the experimental pressures ($P_e$). The coefficient matrix is then recalculated using 2D Legendre polynomials [6]. Using the new coefficients, the pressure quartz recordings are converted into calculated pressure ($P_c$), and a new $MQD$ calculated.

Three "masking" filters were applied to the original calibration points, which are illustrated in Set 1 of Figure 13. The first "mask" (Set 2) removes calibration points at low pressure. The second "mask" (Set 3) removes points at high pressure and low temperature. And the third mask (Set 4), removes the combination of calibration points "masked" in Sets 2 and 3. For each gauge, and with each set, a new coefficient matrix is calculated, and new performance metrics of $P_c$, $[P_c - P_e]$, and $MQD$ are produced.


Figure 13: Illustration of four calibration measurement cases. In Set 1, all calibration measurements are used to calculate the coefficient matrix. In sets 2, 3, and 4, only a proper subset of the calibration measurements, denoted by the gray squares, is used to calculate the coefficients. Red circles denote points that are excluded from the calibration set.

### 3.2.2 Special Considerations

While an atmospheric pressure event is highly unlikely to happen downhole, field operators generally rely on a gauge's reading at atmospheric pressure as a preliminary test that the tool is operating correctly. Simply, a bad reading at atmospheric pressure is an indicator that the gauge has failed, and should be replaced. Therefore, it is important to evaluate the gauge error at atmospheric pressure with each coefficient matrix.

## *3.3 Computational Results*

This section introduces the performance metrics used to evaluate the calibration sets in Figure 13. Namely, the maximal and minimal $[P_c - P_e]$, as well as the calibration's $MQD$, are recalculated. In addition to calculating these metrics on both calibration and calibration check data, two new metrics are proposed which calculate $[P_c - P_e]$ and $MQD$ on the most limited subset of data – i.e., excluding the red pressure/temperature points in Set 4 of Figure 13. The new calibration metrics are Min/Max$[P_c - P_e]_{Sub}$ and $MQD_{Sub}$, respectively.

### 3.3.1 Error in Calculated Pressure, $[P_c - P_e]$

Figure 14 summarizes the error in calculated pressure ($[P_c - P_e]$), using the coefficients from the 4 calibration sets in Figure 13. Note that the measurements are presented in an unwrapped form: the pressure ramp at 200°C is concatenated to the end of the pressure ramp at 60°C.

At first glance, it is not evident how the calibration compares from one set to the next. For one, the original set (Set 1), exhibits the greatest variation in error from one calibration point to the next. The average Max$[P_c - P_e]$ and Min$[P_c - P_e]$ for each set, using calibration and calibration check data, is summarized in Tables 7 and 8.

CONFIDENTIAL

Figure 14: Average $P_c - P_e$ across 10 THQR gauges using the calibration check data.

Table 7: Average Metrics Based on the Calibration Checks of 10 THQR Gauges

| | Set 1 | Set 2 | Set 3 | Set 4 |
|---|---|---|---|---|
| Min/Max$[P_c - P_e]$ (psi) | $-1.92$ / 2.06 | $-1.85$ / 2.26 | $-1.71$ / 2.10 | $-1.63$ / 1.96 |
| Min/Max$[P_c - P_e]_{Sub}$ (psi) | $-1.87$ / 2.05 | $-1.62$ / 2.25 | $-1.66$ / 2.10 | $-1.47$ / 1.96 |
| $MQD$ (psi) | 1.10 | 1.14 | 1.04 | 1.02 |
| $MQD_{Sub}$ (psi) | 1.05 | 1.04 | 0.99 | 0.94 |

Table 8: Average Metrics Based on the Calibration of 32 THQR Gauges

| | Set 1 | Set 2 | Set 3 | Set 4 |
|---|---|---|---|---|
| Min/Max$[P_c - P_e]$ (psi) | $-2.75$ / 3.07 | $-2.51$ / 6.55 | $-6.29$ / 9.61 | $-5.56$ / 9.13 |
| Min/Max$[P_c - P_e]_{Sub}$ (psi) | $-2.71$ / 2.88 | $-2.30$ / 2.85 | $-2.48$ / 2.60 | $-2.15$ / 2.48 |
| $MQD$ (psi) | 1.18 | 1.42 | 1.99 | 1.96 |
| $MQD_{Sub}$ (psi) | 1.16 | 1.08 | 1.07 | 1.01 |

### 3.3.2 $MQD$ and $MQD_{Sub}$

Figure 15 plots the $MQD$ (as classically calculated) and $MQD_{Sub}$ (using only the subset of calibration points in Set 4) averaged across 10 THQR gauges. The $MQD$ does not decrease in Set 2; the exclusion of atmospheric pressure points from the calibration (Set 2 in Fig.13) adversely affects calculated pressure at the same atmospheric regime.

Without "masking" any points (Set 1), the new evaluation metric of $MQD_{Sub}$ is 4.4% lower than the $MQD$. This is not an improvement, but rather just a result of calculating the $MQD$ over a subset of the calibration points. However, on Sets $2-4$, the $MQD_{Sub}$ should be, relative to the cited 4.4% reduction, significantly lower than the $MQD$. Indeed, the $MQD_{Sub}$ using Set 4 provides a 14.5% improvement over the $MQD$. In addition, the $MQD_{Sub}$ tightens the variance on $MQD$ across all sets.

Note that while the removal of atmospheric pressure calibration points (Set 2) deteriorates the $MQD$, it improves the $MQD_{Sub}$.

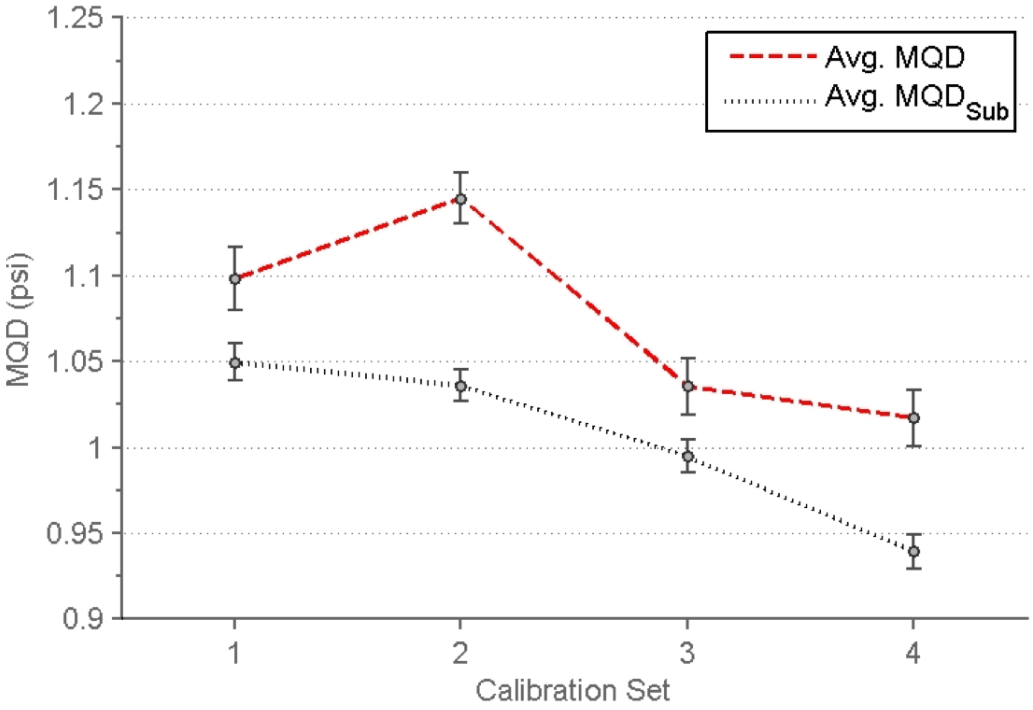


Figure 15: Average $MQD$ and $MQD_{Sub}$ with scaled variances across 10 THQR gauges using the calibration check data.

### 3.3.3 Calibration and Calibration Check Results

The average minimum and maximum calculation errors across each set in Figure 13 are presented in Table 7. The summary of the points in Figure 15 are also included in the table. Note that over the calibration check gauges, Set 4 tightens the range on Min/Max$[P_c - P_e]_{Sub}$ from $-1.92/2.06$ psi to $-1.47/1.96$ psi (0.55 psi or 13.8% reduction).

The same performance metrics presented in Table 7 for the 10 THQR calibration check gauges are presented in Table 8 for the 32 THQR calibration gauges. Note that over the calibration gauges, Set 4 tightens the range on Min/Max$[P_c - P_e]_{Sub}$ from $-2.75/3.07$ psi to $-2.15/2.48$ psi (1.19 psi or 20.5% reduction).

### 3.3.4 Error in Calculated Pressure at Atmospheric Conditions

Recall that atmospheric pressure readings are important namely because they are used by field engineers to check for normal gauge operation. Therefore, each calibration set (Figure 13) is evaluated not only by looking at the holistic metrics (e.g., $MQD$ and $MQD_{Sub}$), but also by inspecting the error associated with gauge readings at atmospheric pressure.

Figure 16 summarizes the pressure calculations at atmospheric pressure and low temperature ($T_e < 50$ °C). There is a visible upward shift in $[P_c - P_e]$ correlated with the calibration temperature ramp. The effect is very likely explained by the hysteretic effect of the quartz response. This hysteresis, however, results in a shift that is both minimal ($|P_c - P_e| < 1.1$ psi) and comparable across the filtered sets.

Ideally, the performance of the gauges at atmospheric pressure is calculated using calibration check data. Note, however, that these points cannot be calculated with calibration check data because the calibration check typically includes pressure ramp measurements at 60 °C and 200 °C: temperatures far beyond what a field operator will find at atmospheric conditions.

## *3.4 Conclusions*

The focus of this chapter was to evaluate the calibration points used for the THQR quartz memory gauges. By calibrating only at a subset of the points currently used in the process, not only is the calibration time reduced (and therefore the cost of calibration per gauge), but the accuracy over likely operating conditions for the gauges is significantly improved.

The removal of unlikely temperature and pressure points from the calibration of THQR gauges improves gauge accuracy over realistic, or likely, operating conditions. New definitions of $[P_c - P_e]$ and $MQD$ are applied only to the subset of calibration points that is not unlikely to happen downhole, denoted by gray squares in Set 4 of

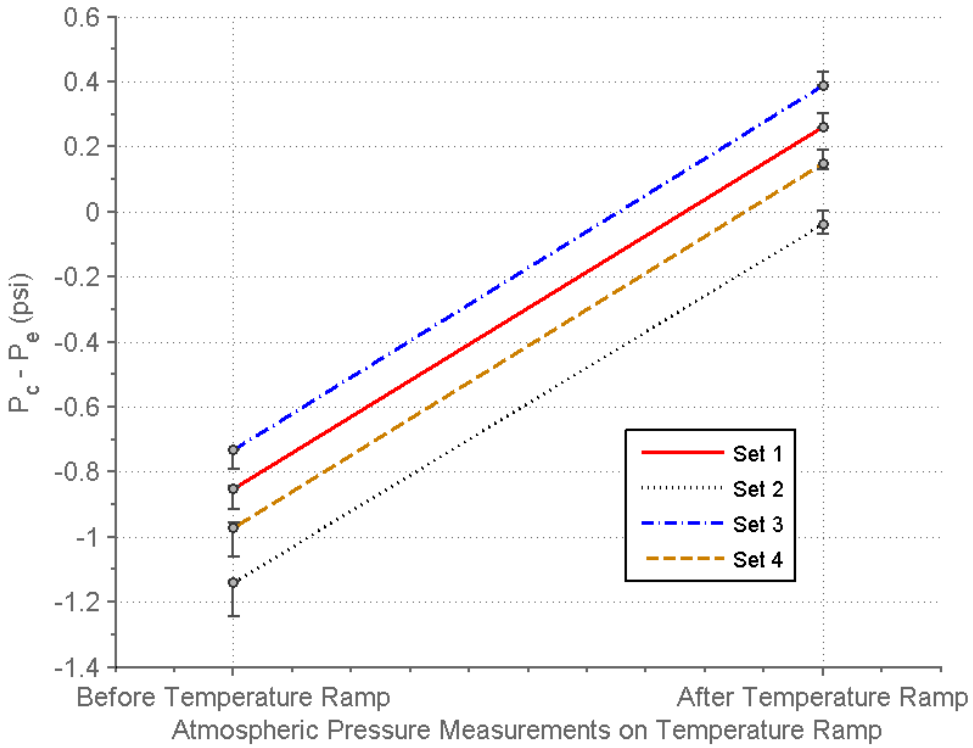


Figure 16: Average atmospheric $[P_c - P_e]$ with scaled Max/Min error bars across 32 THQR gauges using the calibration data.

Figure 13. Using the new metrics, $[P_c - P_e]_{Sub}$ and $MQD_{Sub}$, there is a significant ($> 10\%$) improvement over the same operating conditions:

- On an unfiltered set (Set 1) of calibration measurements, the proposed metric of $MQD_{Sub}$ provides a 0.05 psi (4.4%) reduction over the conventional $MQD$. Over Set 4 of filtered calibration measurements, $MQD_{Sub}$ provides a reduction of 0.16 psi (14.1%). Refer to Figure 15 for $MQD$ and $MQD_{Sub}$ across all sets.

- In addition to increasing accuracy across all filtered sets, $MQD_{Sub}$ also reduces the variance in $MQD$, making it a more rigorous measure of error across THQR gauges. Refer to the scaled variance bars in Figure 15.

- The range on Min/Max$[P_c - P_e]$ is tightened by 1.19 psi (20.5%) in the calibration specifications, and by 0.55 psi (13.8%) in the calibration check results. Refer to Tables 7 and 8 for the average results across 32 calibration gauges and

10 calibration check gauges.

- The filtering of unlikely points has little to no negative impact on the gauge performance at atmospheric pressure; operators can still perform failure checks on gauges while on the job, in the field. Refer to Figure 16 for $[P_c - P_e]$ at atmospheric pressure across all sets.

### 3.4.1 Future Work

In Figure 15, $MQD_{Sub}$ drops as the number of unlikely downhole calibration points that are removed from the coefficient matrix calculation increases. As coefficients are calculated over fewer pressure points, the calibration $MQD$ and $MQD_{Sub}$ tend to improve. Future work should seek to investigate that trend and its limit for THQR gauges. This would also require having a more detailed map of the pressure/temperature conditions that the THQR typically experiences downhole.

Another point of interest is a comparable evaluation of other calibration sets for different gauge models (e.g., TUPR and TQPR). Finally, this chapter's treatment of calibration points was binary (elimination/retention of calibration point); one suggested topic for future work is associating a weight to calibration points, and therefore force a strong fit to calibration points of greater importance or relevance.

# CHAPTER IV

# TIME-DOMAIN ALIGNMENT OF MEMORY GAUGE MEASUREMENTS

The challenge of non-linear alignment of two or more signals is a recurrent theme in a wide range of signal processing topics that extend across numerous fields: speech recognition [29], audio recording alignment [10], text segmentation [11], online signature matching [15, 27], and by extension, any application where similar, out-of-phase signals must be re-accommodated by some kind of elastic shift. The overarching quality across the different applications is that while signal (mis)alignments are qualitatively evident, the manual segmentation and alignment of any large signals proves to be an ad-hoc exercise that is both impractical and expensive.

Quartz memory gauges are no exception to the challenges of signal alignment. Memory gauge data for a 15-day well test can sample upwards of 30,000 triplets (i.e., time stamp, pressure, and temperature), or a total of 90,000 data points. With higher sample rates, memory gauges can sample upwards of 130,000 triplets (390,000 data points) to a maximum of 5,000,000 triplets (15,000,000 data points) [1]. The inclusion of multiple gauges in a job increases this number by the same factor. The sheer volume of data in these generalized estimates motivates an efficient, automated technique to align measurements for two or more gauges. The rest of this chapter describes the treatment of memory gauge signals with pre-processing techniques to minimize processing cost without loss of information, and subsequent time-domain alignment through a non-linear normalizing technique known as dynamic time warp DTW. Finally, it is duly noted that this chapter borrows heavily from [10, 29].

## *4.1 Introductory Treatment of Misaligned Signals*

After a well test is completed, the data is extracted from each tool, stored in a central data base, and made available to a variety of research, manufacturing, and engineering teams for the purposes of well interpretation, performance validation, case studies, etc.. With few exceptions, this data is for the most part raw, which means it lacks any time alignment. In the case of multiple pressure gauges, time misalignment is due to a combination of factors:

- Gauges programmed to record at *different sample rates* to improve the collective richness of measurement data both in time resolution and length of measurement campaign,
- Gauges set to turn on/off at different measurement campaign stages, incurring variable drifts depending on the *different operational modes*,
- Drifts associated with *long-term lifetime of gauge*,
- Non-linear response of clock quartz oscillation to *changes in temperature*,
- Random, zero-mean, *short-term variations in clock drift* due to natural oscillation in environment conditions and in quartz response

The combination of these misalignments can be approximated with three kinds of time-domain perturbations on a reference signal, $f(t)$:

1. Initial time offset, $t_{\text{offset}}$: $f(t - t_{\text{offset}})$
2. Exponential time drift with offset, $t_{\text{start}}$, and growth rate, $t_{\text{rate}}$: $f(t \cdot e^{\frac{t_{\text{start}} - t}{t_{\text{rate}}}})$
3. Periodic time drift with amplitude, $t_{\text{amp}}$, and frequency, $t_{\text{freq}}$: $f(t_{\text{amp}} \cdot sin(t_{\text{freq}} \cdot t))$

Figure 17 illustrates how misalignments might accumulate across two time series, and suggests how the dynamic time warp might index them – i.e., find the aligning time warp.

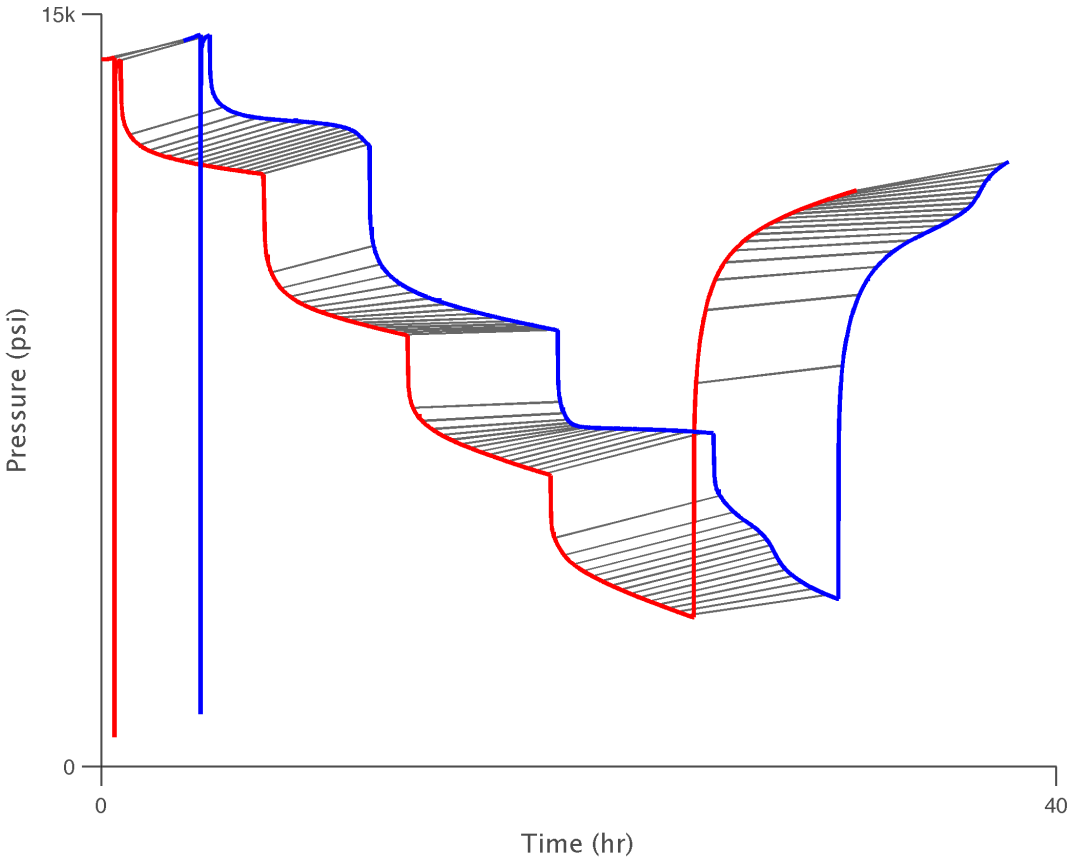


Figure 17: Reference pressure signal (red) and warped pressure signal (blue).

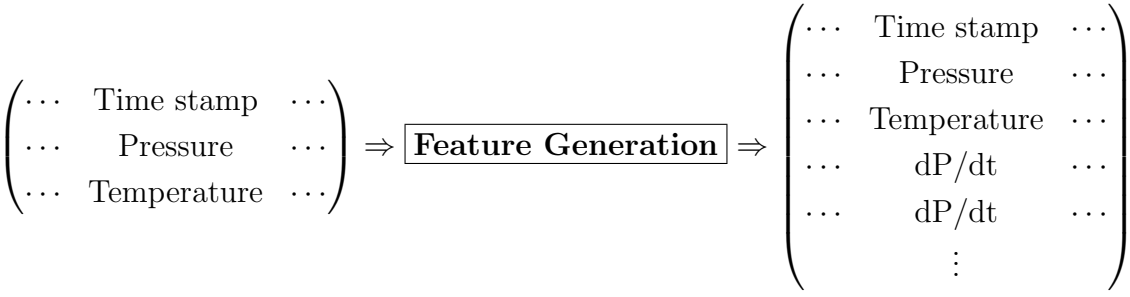


Figure 18: Basic cross-feature vector for a memory gauge signal (left) and derived cross-feature vector (right).

### 4.1.1 Feature Vector Generation

Some applications require that discrete features be extracted from the signals before these can be aligned. For instance, for audio alignment, Filos proposes methods of windowing and extracting time- and frequency-domain features – e.g., short-term energy, first derivative w.r.t. time, MFCC coefficients, and Delta coefficients – from a common .wav audio file [10]. The frequency-domain features capture information that is not necessarily described by the time-domain amplitude envelope of the signal.

When dealing with pressure and temperature signals such as those provided by a quartz pressure gauge, it is not necessary to expend much effort in extracting new features. However, that does not mean that the proposed alignment method cannot profit from additional features. Figure 18 shows a basic feature vector (left) and suggests a derived feature vector (right). Preliminary DTW simulations were run with the inclusion of first pressure and temperature derivatives in the feature vectors. While these simulations showed little to no improvement in the alignment, this was not an exhaustive study of feature extraction.

### 4.1.2 Time-Domain Homogenization

Time-domain homogenization in pre-processing is not a requirement for DTW. However, resampling both pre-aligned signals with a common clock helps mitigate time-domain normalization asymmetries that may arise if signals are not sampled at comparable rates. For instance, it is common for multiple gauges to be lowered in the drill string, and for these to be programmed to sample at different rates to provide both high time resolution and extended-term measurement campaigns.

Time-domain homogenization for two gauges means aggregating all the unique time samples from each gauge into one common clock, $C$. After parsing the signals for the two gauges, $X'$ and $Y'$, $C$ is given by

$$C = C_{X'} \cup C_{Y'} \tag{15}$$

where $C_{X'}$ and $C_{Y'}$ are the time stamp vectors for each gauge, respectively. Each signal is then interpolated at the time stamps in $C$ to produce the signals $X$ and $Y$:

$$X = \begin{pmatrix} x_{1,1} & x_{1,2} & \cdots & x_{1,N_x} \\ x_{2,1} & x_{2,2} & \cdots & x_{2,N_x} \\ \vdots & \vdots & \ddots & \vdots \\ x_{M_x,1} & x_{M_x,2} & \cdots & x_{M_x,N_x} \end{pmatrix} \quad Y = \begin{pmatrix} y_{1,1} & y_{1,2} & \cdots & y_{1,N_y} \\ y_{2,1} & y_{2,2} & \cdots & y_{2,N_y} \\ \vdots & \vdots & \ddots & \vdots \\ y_{M_y,1} & y_{M_y,2} & \cdots & y_{M_y,N_y} \end{pmatrix} \tag{16}$$

where each column is a feature vector sample that corresponds to a unique time stamp in $C$, and each row comprises one feature across the entire measurement campaign. This is a good place to note that the first row corresponds to the first feature; time stamps are herein excluded from the signal feature vectors. Signal definitions in Eq. 16 apply regardless of whether they have been homogenized in time.

### 4.1.3 Feature Vector Normalization

Dynamic time warp relies on a distance function to determine the warp path that minimizes the distance between two signals. However, features do not necessarily have the same mean and variance, which means that if the distance function used performs no vector normalization, the feature with large mean and variance will dominate the cost function. For instance, throughout the course of a drill stem test, pressure may vary 5,000+ psi, while temperature may vary no more than 50°F. In normalizing, each element in a feature vector is scaled by

$$\tilde{x}_m = \frac{\bar{x}_m - \mu_{x_m}}{\sigma_{x_m}} \tag{17}$$

where $\mu_{x_m}$ is the feature mean, $\sigma_{x_m}$ is the feature standard deviation, and for any feature vector in $x$ there is an equivalent row feature vector in $y$ such that

$$\begin{aligned} \bar{x}_m &= [x_{m,1}, x_{m,2}, \ldots, x_{m,N_x}] \; \forall \; m \in 1 \ldots M_x \\ \bar{y}_m &= [y_{m,1}, y_{m,2}, \ldots, y_{m,N_y}] \; \forall \; m \in 1 \ldots M_y \end{aligned} \tag{18}$$

Signals should have the same number of features, such that $M_x = M_y$ in the signal definitions in Eq. 16 as well as in the feature vector definitions in Eq. 18.

### 4.1.4 Feature Vector Weights

Once normalized, the feature vectors can be weighted according to application priority. Feature vector weights help improve the time-normalization effort by mitigating the error contributed by "weaker" feature vectors. A feature vector may be "weak" for a number of reasons, such as being less reliable due to reduced measurement accuracy, resolution, or physics.

Note that in pressure gauges, the two main feature vectors – i.e., pressure and temperature – are not of equal relevance on the basis of measurement physics alone. For instance, gauges that are placed within close quarters of each other are expected

to have highly correlated pressure readings. The temperature readings, however, will exhibit less correlation. The most obvious reason for this is that the velocity of pressure propagation is far greater than that of temperature propagation. Results for tested feature vector weights are presented and discussed in further detail in Section 4.4.2.

As gauges are placed further apart from each other – e.g., in pressure gradient measurements along the drill string – the time offset expected from the pressure wave propagation can easily be accounted for. On the other hand, modeling temperature propagation in a well becomes an increasingly difficult and unreliable task as distance between gauges increases. In such a situation, the benefits of feature vector weights become more evident.

## *4.2 Naïve Dynamic Time Warp*

The dynamic time warp algorithm distinguishes itself as the basis of gait recognition algorithms for its efficient calculation of time-domain series and identification of an elastic shift that minimizes the dissimilarity between signals [12]. In short, the naïve, unadulterated DTW process consists of characterizing distance between two signals through a similarity matrix, and calculating the warp path that minimizes the accumulated distance between the endpoints of this same matrix.

### 4.2.1 Signal Similarity Matrix

At the core of a similarity matrix is a function or metric that measures the distance between two points. Any such distance measure obeys the properties of non-negativity, symmetry, and the triangle inequality [9]. The squared Euclidean distance was selected for analysis, and implemented in its factored form,

$$\begin{aligned} D \in \mathbb{R}^{N_x \times N_y} : d(\bar{x}_i, \bar{y}_j) &= \|\bar{x}_i - \bar{y}_j\|^2 \\ &= \|\bar{x}_i\|^2 + \|\bar{y}_j\|^2 - 2 \cdot (\bar{x}_i \cdot \bar{y}_j) \end{aligned} \tag{19}$$

where every sampled feature vector in $X$, $\bar{x}_i$, is compared to every sampled feature vector in $Y$, $\bar{y}_j$, and sample feature vectors are defined as

$$\begin{aligned} \bar{x}_i &= [x_{1,i}, x_{2,i}, \ldots, x_{M_x,i}]^T \; \forall \; i \in 1 \ldots N_x \\ \bar{y}_j &= [y_{1,j}, y_{2,j}, \ldots, y_{M_y,j}]^T \; \forall \; j \in 1 \ldots N_y \end{aligned} \tag{20}$$

### 4.2.2 Time Warp Path

Once a similarity matrix has been calculated – for an example, refer to Figure 23– any given warp path, $W$, has a weighted accumulated cost given by

$$d_W(X, Y) = \sum_{(i,j) \in W} d(\bar{x}_i, \bar{y}_j) \cdot w_{i,j} \tag{21}$$

where $w_{i,j}$ is a weighting coefficient. The warp path that minimizes the cost function is defined as $\tilde{W} \in \mathcal{W}$, and is given by

$$d(X, Y) = \min_{\tilde{W} \in \mathcal{W}} \frac{d_W(X, Y)}{\sum w_{i,j}} \tag{22}$$

where the weighted accumulated cost in Eq. 21 is normalized by the sum of the weights along the warp path. Eq. 22 can be easily solved by dynamic programming (DP) if the normalization term in the denominator is independent of warping function, and therefore the problem is rewritten in the same form as in [29]:

$$d(X, Y) = \frac{1}{\sum w_{i,j}} \min_{\tilde{W} \in \mathcal{W}} d_W(X, Y) \tag{23}$$

Some restrictions apply to the minimization problem in Eq. 23:

- *Boundary conditions* force the endpoints of the warp function to the diagonals of the similarity matrix, or alternatively, the time-aligned signals must be coincident at the endpoints,
- *Continuity conditions* limit the warping path to adjacent signal sample frames in both $i$ and $j$, and

- *Monotonicity conditions* guarantee that time-aligned signals obey unidirectional, nondecreasing time.

In addition to detailing these conditions, Sakoe and Chiba [29] and Filos [10] include a *slope constraint* and *adjustment window condition* that are discussed in greater detail in Section 4.3.1 as tuning parameters of the dynamic programming in the naïve DTW.

## *4.3 Dynamic Programming*

In spite of the aforementioned conditions, there are exponentially many warping paths, where the solution space complexity is of $O(N_x N_y)$. By using dynamic programming, however, efforts can be focused on finding the minimum cost path by solving Eq. 23 at a reduced processing requirement. In this section, two methods are introduced to reduce the solution space, and therefore, the computational requirement: slope constraint and warp path bands. A third implementation parameter, that of weight coefficient form, is presented. Finally, the DTW algorithm is described using the predefined implementation parameters.

### 4.3.1 Tuning Parameters in Dynamic Programming

#### *4.3.1.1 Slope Constraint*

In some applications, it is ill-advised to allow the for the search for minimizing path, $\tilde{W}$ in Eq. 23, to be unconstrained in slope. A steep warp gradient might yield a forced fit between independent and uncorrelated segments. Conversely, restriction of any reasonable gradient would remove the elastic properties of the path, and therefore reduce the DTW to the likes of a linear shift or worse if the path is forced to the diagonal $i = j$. In [29], Sakoe and Chiba define the gradient constraint as

$$P = \frac{k_{\text{diagonal}}}{k_{i \text{ or } j}} \tag{24}$$

such that if the warp function moves $k_{i \text{ or } j}$ steps in a horizontal or vertical direction, it cannot continue in that direction until it moves $k_{\text{diagonal}}$ steps along the diagonal. Therefore, the larger $P$, the more restricted the slope, where $P = \infty$ would yield a path along the diagonal. For $P = 0$ the path is unrestrained.

As slope restriction increases, the computational complexity of the DTW decreases; one effective way of reducing processing time. In quartz pressure gauges the drifts on clocks does not come remotely close to an hour over the span of 15 days, which means that the optimal path will stay relatively centered along the diagonal and, generally, a restricted slope will not deteriorate alignment. However, the simulation in Section 4.4 grossly exaggerates signal misalignment in the interest of evaluating an improbable worst-case scenario. Therefore, a path search with no slope restriction, or $P = 0$, is used in the DTW simulation.

#### *4.3.1.2 Warp Path Bands*

When optimal warp paths are expected to run near to the diagonal, two DP features can be tuned accordingly to reduce computational complexity. The first feature, slope restriction, has already been discussed in Section 4.3.1.1. A second feature is that of warp path bands. By adjusting the boundary conditions in the dynamic programming algorithm, the search for the optimal warp path can be limited to a subset of the similarity matrix. Two such subsets are introduced in this section: the Sakoe/Chiba Band and the Itakura Parallelogram Band. These are illustrated in Figure 19.

Henniger and Muller [15] cite an optimal empirical Sakoe/Chiba band width of 10% the maximal side length of the similarity matrix, or $\max(N_x, N_y)$. The main priority of this chapter is neither dealing with computational complexity or processing time (within reason). That said, for gauges that have not suffered from catastrophic failure to the clock, the warp function that aligns memory gauge signals will remain

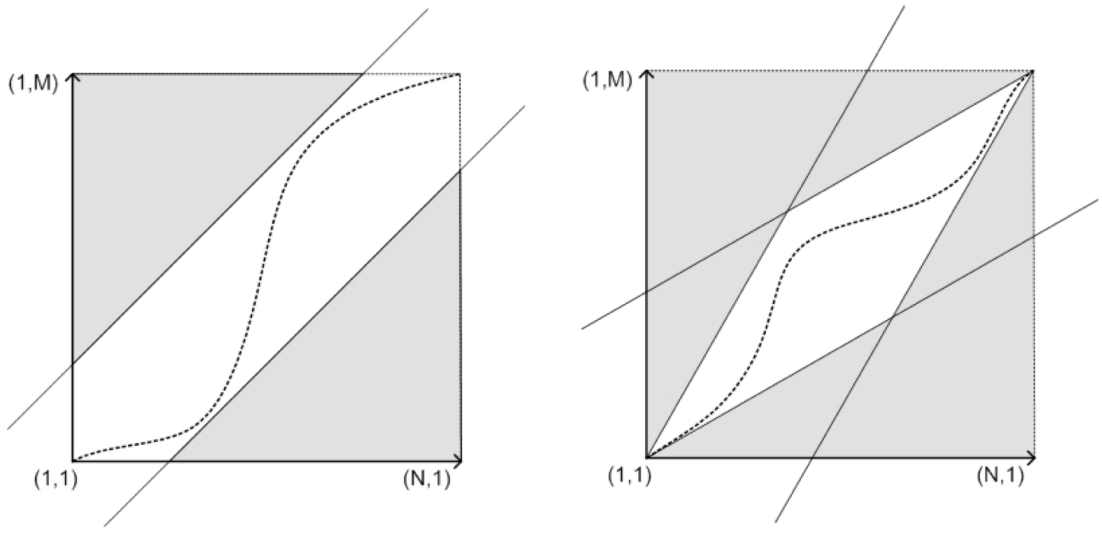


(a) Sakoe/Chiba Band (b) Itakura Parallelogram Band

Figure 19: Illustration of two types of warp path constraints: (a) Sakoe/Chiba and (b) Itakura. Borrowed from [32].

namely along the diagonal. No band restriction was used in the DTW simulation, though the Sakoe/Chiba bands should satisfy the requirements for this application.

#### *4.3.1.3 Weight Coefficient Form: Symmetric vs. Asymmetric*

In [29], Sakoe and Chiba present two typical definitions for the weight coefficient in 21: symmetric and asymmetric. Further, Sakoe and Chiba conclude that the symmetric DP-matching is superior over asymmetric DP. In the symmetric form, the following weighting coefficient applies:

$$w_k = (i_k - i_{k-1}) + (j_k - j_{k-1}) \; \forall \; k \in W \tag{25}$$

In words, the weight for a path at a given cell is equal to the sum of the vertical cells (path moves along $i$) and the horizontal cells (path moves along $j$) transcurred over the last two indices of that path, $k$ and $k-1$. For a path that moves along the diagonal, $w = 2$; otherwise, $w = 1$.

### 4.3.2 Algorithm

Solving for the minimizing path in Eq. 23 can be done by the recurrent calculation in ascending $i$ and $j$ of the distance accumulated by a current cell and its adjacent neighbors. For the case of unconstrained slope ($P = 0$), the DP equation is

$$\gamma(i,j) = d(\bar{x}_i, \bar{y}_j) + \min \begin{bmatrix} \gamma(i-1, j-1) \\ \gamma(i-1, j) \\ \gamma(i, j-1) \end{bmatrix} \tag{26}$$

A thorough treatment of the dynamic programming theory and implementation for varied slope constraints is provided by Sakoe and Chiba [29], Keogh and Ratanamahatana [20], and Filos [10].

## *4.4 DTW Evaluation*

Pressure and temperature measurements from a drill stem test field gauge were used as the basis for the signals used to evaluate the dynamic time warp algorithm. The reference pressure signal (red curve in Figure 17) was delayed and elastically shifted using a combination of time-domain warps (as described in Section 4.1) to produce the time warped pressure signal (blue curve in Figure 17).

Two points merit note:

1. The signals used in the DTW evaluation are identical to those illustrated in Figure 17, with the exception that the warped signal in this figure was modified in pressure levels for illustration purposes, and

2. With the exception of warped time, the evaluated signals are identical.

Table 9: DTW Calculation Parameters

| Simulation Parameters | Parameter Values |
|---|---|
| Samples per Hour | 15, 30, 60, 120, 240 |
| P/T Feature Vector Weights | 100/0, 75/25, 50/50, 25/75, 0/100 |
| Median Filter Order | 1, 3, 5 |

Table 10: DTW Alignment Metrics

| Alignment Metrics |
|---|
| Pressure Score |
| Temp. Score |
| Average Score |
| Processing Time |

### 4.4.1 DTW Calculation Parameters, Alignment Metrics, and Preliminary Results

DTW was calculated by varying three parameters: resampling factor (i.e., desired samples per hour), feature vector weights, and median filter order. With each DTW calculation, four alignment metrics were calculated: pressure score, temperature score, average of pressure and temperature scores, and processing time. The calculation parameters and alignment metrics are summarized in Tables 9 and 10.

The pressure and temperature scores quantify the sum of the squared Euclidean distance between the aligned signals normalized by the number of points in the signals. These metrics are defined by

$$\text{Pressure Score} = \frac{d(X_P, Y_P)}{\sum_{k \in \tilde{W}} k} \tag{27a}$$

$$\text{Temperature Score} = \frac{d(X_T, Y_T)}{\sum_{k \in \tilde{W}} k} \tag{27b}$$

$$\text{Average Score} = \frac{\text{Pressure Score} + \text{Temperature Score}}{2} \tag{27c}$$

Preliminary DTW results were used to evaluate which parameters had the greatest

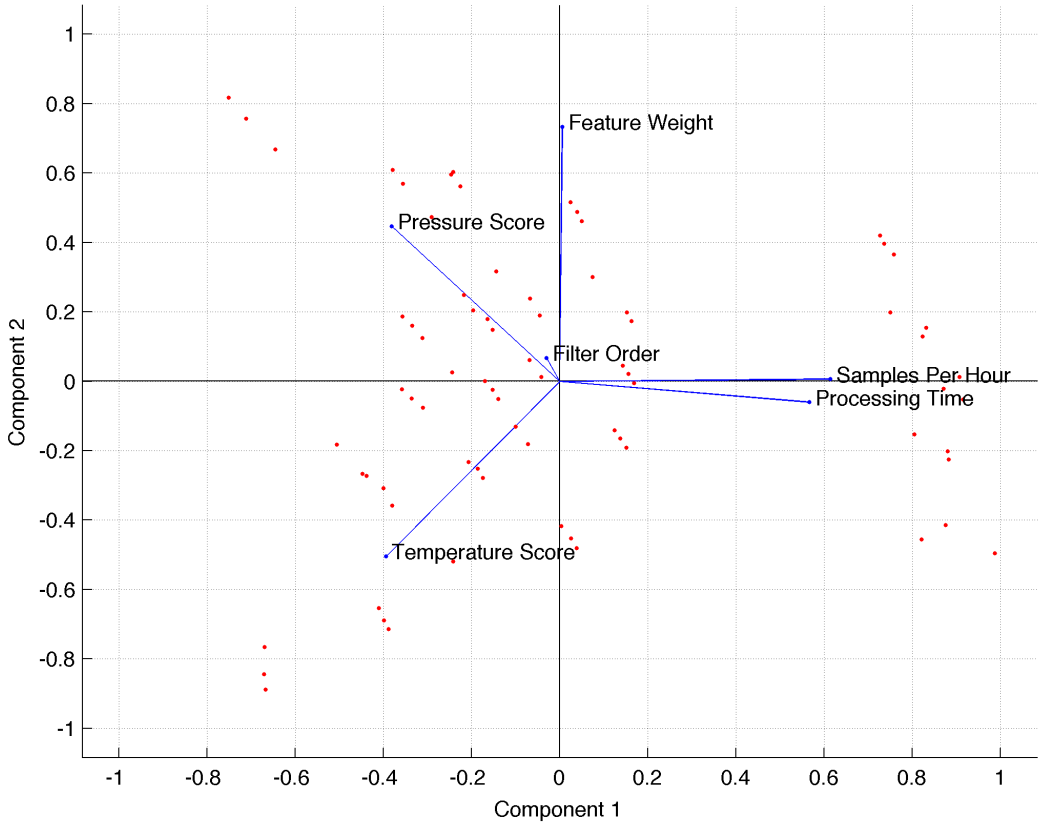


Figure 20: Principal Component Analysis (PCA) for DTW parameters and alignment metrics.

effect on alignment metrics. As expected, pressure and temperature scores were correlated with both feature vector weight and resampling factor. Computational complexity, and therefore processing time, were directly correlated with resampling factor. Median filter order had a relatively limited effect on both scores and processing time. These results, which were observed using principal component analysis (PCA), are included in Figure 20.

### 4.4.2 Results

Based on the preliminary DTW calculations and the results in Figure 20, a 5th order median filter was implemented and the DTW path was recalculated over the parameters in Table 9. The main relations between sample rate, feature weights,

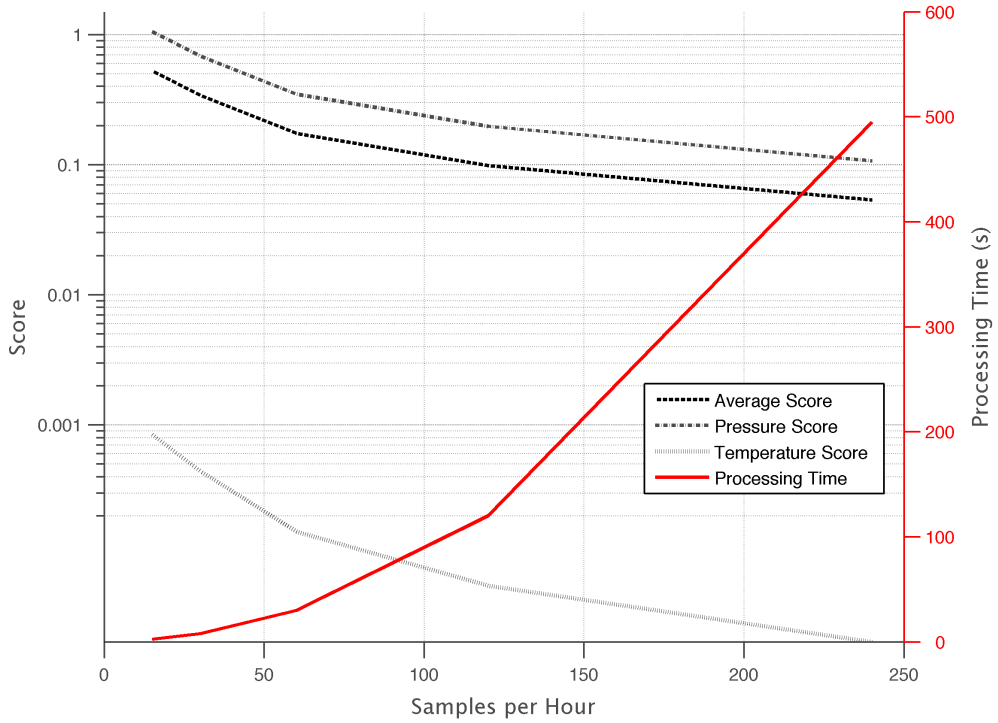


Figure 21: Effect of signal sample rate on time-normalization score and processing time.

scores, and processing times are summarized in Figures 21 and 22.

The benefits of increasing the sample rate in Figure 21 meet expectations: improvement of scores at a diminishing rate with increase in samples per hour. Processing time increases exponentially due to a combination of increased CPU and memory requirements. With limited processing power, a suggested, albeit subjective sample rate of 60–120 samples per hour is recommended.

The results in Figure 22 shed some additional light on the topic of feature vector "weakness", a concept introduced in Section 4.1.4. The temperature signal in the simulated DTW exhibits a higher rate of local variance, which in this case translates to a greater number of distinct features that, relative to the pressure signal, provide improved resolution in the alignment effort. This helps explain why the pressure score in Figure 22 is maximal when the temperature feature has a weight of 75%.

The warp function illustrated in Figure 23 was calculated with a rate of 120

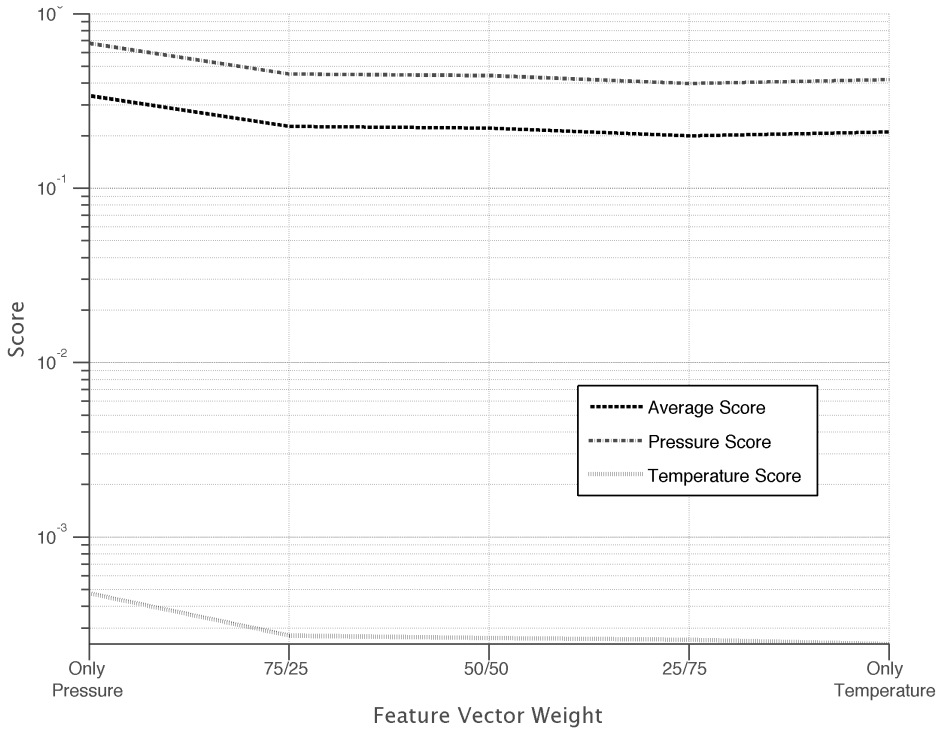


Figure 22: Effects of feature vector weight on time-normalization score.

samples per hour and pressure/temperature feature weight of 25%/75%, respectively. The resulting pressure, temperature, and average scores were 0.1651, 0.00005, and 0.08358, respectively. Some of the misalignment elements discussed in Section 4.1 – e.g., sinusoidal time shift – are apparent in the optimal warp that runs diagonally across the similarity matrix in Figure 23. The path shows the correspondence in time indices between the misaligned signals (red and blue curves).

## *4.5 Conclusions*

In the following section, an overview of the results provides insight into the general success of DTW in the alignment of memory gauge measurements. Particular points are made on fine tuning the DP algorithm for improved results. Finally, methods are suggested that may improve the näive DTW in memory gauge alignment, including a thorough evaluation of feature treatment, faster DTW algorithms, and alternative time-series alignment techniques.

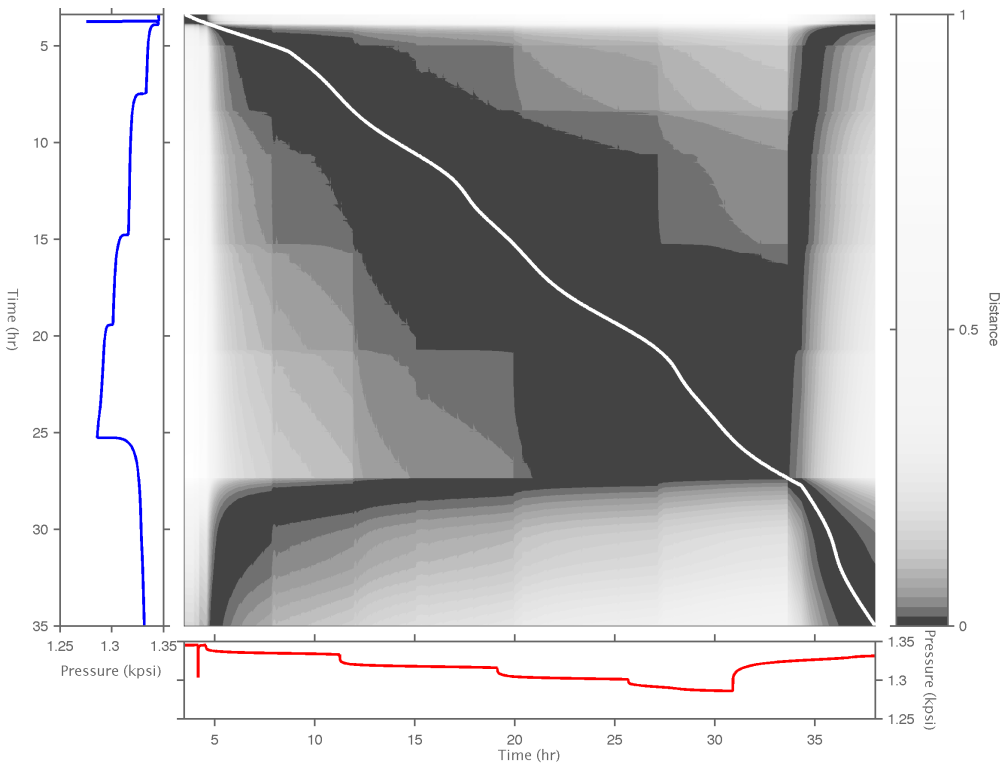


Figure 23: Similarity matrix between misaligned signals (in red and blue) and optimal warp path (in white).

### 4.5.1 Analysis of Results

It is evident from the simulations and alignment scores calculated in Section 4.4.2 that, even in the presence of excessive and unrealistic clock drifts, DTW is a robust technique capable of realigning both pressure and temperature signals. Only two parameters in the dynamic programming algorithm presented in Section 4.3 have a moderate to significant effect on the alignment: signal (re)sample rate and feature weights. But even a poorly tuned implementation is likely to yield an improvement in signal alignment.

Extracted features, such as those introduced in Section 4.1.1, have no positive effect on alignment. The results suggest that the the information necessary for proper alignment is fully contained in the pressure and temperature signals; there is no evidence suggesting that additional features need be generated.

As expected, higher signal sample rates result in better alignments. A surprising result is that more useful information can be carried in a temperature signal than in a pressure signals itself. Surprising, albeit not counterintuitive: in the case of the tested signals, the temperature had greater local variance and therefore greater number of distinct events than the pressure signal. The greater the number and distribution of local events, the greater the alignment resolution.

Finally, this chapter has detailed the process of calculating the tuning parameters for the particular set of tested signals. These results, however, cannot be generalized in their current presentation. Well tests deliver great variation in pressure and temperature profiles, which means that tuning parameters may need adjusting to obtain an optimal alignment.

### 4.5.2 Future Work

This chapter presents the foundation for a "smarter" implementation of the näive DTW algorithm in the area of memory gauge measurements. Given the relative simplicity of the pressure and temperature signal alignment problem, future work should not only focus on improving alignment quality, but also in reducing the computational complexity and run-time processing requirement.

The optimization parameters introduced in Section 4.3.1 deserve a more thorough evaluation. Future research efforts in this area should quantify the tradeoff between processing time and alignment quality as the slope constraint is increased. Additionally, the warp path bands may vastly improve the run-time processing without hurting alignment quality. Clock drift is rarely as excessive as it was simulated in this chapter. In practice, the optimal warp path will run within a narrow band of the similarity matrix diagonal. Such a problem can both afford and profit from the inclusion of a carefully selected constrained slope and warp path bands.

While evidence suggests that the pressure and temperature signals carry most of the information necessary in signal alignment, there is interest in further understanding the utility of raw and derived features, alike. Computational complexity for DTW is dominated by samples per feature, and not by length of feature vectors. With that in mind, there may be some practical and academic merit in defining and evaluating additional features that include, but are not limited to, frequency-domain feature generation.

The proposed DTW would be significantly enhanced by automated parameter tuning. One example of automation is developing a new metric that quantifies the amount and distribution of distinct events in each feature. This metric can be used to prioritize or rate features and, subsequently, be mapped to a feature vector weight.

Finally, the next generation of DTW in gauge signal alignment may profit adopting some of the more recent work in DTW hybridization, fast algorithm implementation,

and data imputation handling. Relevant work in "FastDTW" has been introduced by Salvador and Chan in [30]. In [12], Fu et al. propose a new time warping technique that can handle both DTW and Universal Scaling (US) simultaneously. And in [7], Cismondi et al. provide a thorough review of the challenges in large sample sets of time series, and provide insight as to potential approaches to alignment and statistical imputation.

# CHAPTER V

# LONG DURATION JOB AUTONOMY MODEL

Accurately predicting how long a pressure tool will last under well conditions is vital to select the most appropriate tool for a job. To a first order, tool autonomy consists of the consumption of a tool and the capacity of the battery that is powering it; both consumption and capacity are functions of the tool's sampling rate and operating temperature. In addition, the tool is also limited by its memory, which has an autonomy that is a function of sampling rate and, to a lesser degree, memory compression due to pressure/temperature gradients. The operator often negotiates the trade-off between the duration of the job and the desired sampling rate. It is therefore particularly useful to model the autonomy of combinations of tools and batteries as functions of sampling rate and temperature.

After a thorough review of existing autonomy data for Signature$^{TM}$ gauges (THQR/TQPR/TUPR) and batteries (SubC 150/175/210), this chapter proposes a tool autonomy estimation model comprised of three major subsystems: memory autonomy, tool consumption, and effective battery capacity. The model of the effective battery capacity is developed using existing battery capacity tests, and this is divided by the tool consumption in order to produce a memory-less tool autonomy. The memory autonomy is calculated using known data compression rates. The final tool autonomy is the minimum of the memory-less tool and the memory autonomy for every sample rate and temperature.

Finally, a surface response methodology recommendation is provided to test batteries over the parameter space of sample rates (2, 10, and 60 sec) and temperatures (25, 100, 125, 150, 175, and 210°C), keeping current loads comparable to those of the

Signature$^{TM}$ tools, and keeping all other test parameters (e.g., depassivation, ramp-up, etc.) constant. [redacted]

## *5.1 Strategy*

There is a wealth of experimental battery and tool autonomy data that has been produced using varied test conditions and setups. For example, the capacity of batteries is often calculated with simulated tool consumption at different pulsed current loads and test temperatures. In these simulated conditions, the sampling rates and loads for active/standby modes are not always consistent from one test to the next. Battery depassivation routines sometimes vary between tests. Some tool autonomy tests have also been carried out running an actual tool (versus simulated consumption). In addition to battery tests, the tools are tested for active and standby consumption at different temperatures. The variations in battery tests, however, make it difficult to derive the effects of any one parameter on autonomy.

Given the difficulties inherent in isolating the effects of single test conditions on performance, the long term autonomy model relies on estimating an effective battery capacity (A-hr), using experimental active/standby tool consumptions, and specifying sampling rate and operating/well temperature. The effective battery capacity, which can be estimated from existing battery autonomy tests, differs from the theoretical capacity in that it captures losses over time (i.e., an approximation of self-discharge), pulsing rate inefficiencies, and losses in capacity at different temperatures (i.e., an approximation of chemical inefficiencies).

The tool memory also plays a role in tool autonomy: at high sampling rates ($5 <$ sec) the tool memory is likelier to deplete before the battery. The memory autonomy

is not as variable as the battery autonomy and can more accurately be estimated even with variable compression rates.

Given a tool sample rate and operating temperature, the effective battery capacity and tool consumption are sufficient to estimate the tool autonomy assuming there is no memory limit. This "memory-less" autonomy is given by

$$\text{Memory-less Tool Autonomy [hr]} = \frac{\text{Battery Capacity [Amp} \cdot \text{hr]}}{\text{Avg. Tool Consumption [Amps]}} \tag{28}$$

Memory autonomy is calculated independent of the memory-less tool autonomy in Eq. 28 for each sampling rate; the lesser of the two autonomies (memory-less tool autonomy versus memory autonomy) determines the effective tool autonomy.

## *5.2 Memory Autonomy*

The memory autonomy is estimated using the memory capacity, the memory consumption of a reading (i.e., a temperature and pressure pair), and the sampling rate. There is also variance in the memory autonomy due to the compressibility of each recorded pair. Temperature and pressure pairs are differentially recorded and encoded: a big temperature difference from one reading to the next will require more memory than a small temperature difference. The same effect of compressibility applies to pressure readings. [redacted] These two bounds comprise the variance in the memory autonomy model. Tables 11 and 12 summarize the data necessary to evaluate the memory autonomy.

Table 11: Memory Specification of Signature$^{TM}$ Gauges

| Gauge Type | Flash Memory Cells | Cell Memory (MB) | Recording Blocks ($B_i$) |
|---|---|---|---|
| [redacted] | [redacted] | [redacted] | [redacted] |
| [redacted] | [redacted] | [redacted] | [redacted] |

Table 12: Parameters of Memory Autonomy

| Variable | Notation | Comments |
|---|---|---|
| Time (hr) | t | |
| Sampling Rate (sec) | r | [redacted] |
| Pressure Memory Size (Bytes) | $M_P$ | [redacted] |
| Temperature Memory Size (Bytes) | $M_T$ | [redacted] |
| Battery Memory Size (Bytes) | $M_1$ | [redacted] |
| Number of Recording Blocks | $B_i$ | Tool dependent (Table 11) |

Several significant metrics that lead up to the total percentage of memory consumed are derived from the parameters in Tables 11 and 12:

$$\text{Number of P/T Pairs: } N_{P/T} = \frac{t \cdot 3600}{r} \tag{29a}$$

$$\text{Memory Used by P/T Pairs (Bytes): } M_{P/T} = N_{P/T} \cdot (M_P + M_T) \tag{29b}$$

$$\text{Flash Memory Consumed by P/T Pairs (\%): } F_{P/T} = \frac{M_{P/T}}{1024 \cdot B_i} \cdot 100 \tag{29c}$$

$$\text{Number of Battery Points: } N_B = \frac{t \cdot 60}{10} \tag{29d}$$

$$\text{Memory Used by Battery Points (Bytes): } M_B = N_B \cdot M_1 \tag{29e}$$

$$\text{Flash Memory Consumed by Battery Points (\%): } F_B = \frac{M_B}{B_i \cdot 1024} \cdot 100 \tag{29f}$$

$$\text{Total Flash Memory Consumed (\%): } F = F_{P/T} + F_B \tag{29g}$$

Solving for time in Eqs. 29a – 29g yields

$$t = \frac{F \cdot r \cdot (B_i \cdot 1024)}{360,000 \cdot (M_P + M_T) + 600 \cdot M_1 \cdot r} \tag{30}$$

The memory autonomy defined in Eq. 30 is graphed in Figure 24 using the number of recording blocks for each tool ($B_i$). The THQR sampling rate should not exceed 5 seconds due to excessive drift on the clock during standby mode. However, the THQR's battery guard activates a sample rate of 600 seconds when the battery is low.

The memory autonomies mark when the tool has consumed 90% of its memory. At this point in time, the memory guard mechanism activates and the sampling rate is reduced to conserve memory.

## *5.3 Tool Consumption*

The tool consumption is a function of both sample rate and temperature. The current model uses tool consumption measurements from 25°C up to rated temperature for each tool. This current consumption is independent of the battery pack used to power the tool. Required measurements to model tool consumption are the current load in standby mode, and in all the active modes [redacted] Figure 25 illustrates the tool consumptions for THQR, TQPR, and TUPR gauges.

The active and standby current loads at each temperature and sampling rate are used to calculate the average consumption. This average consumption is described by the pseudo-code in Figure 26.

[redacted]



(b) Memory Autonomy of TQPR/TUPR Gauges

Figure 24: Memory autonomy of (a) THQR and (b) TQPR/TUPR gauges at fixed sample rates. Note logarithmic scales.

[redacted]

## 5.4 Battery Capacity

Battery capacity is fundamental in the proposed model. Of the three main sub-models – i.e., memory autonomy, tool consumption, and battery capacity – this last one requires the most resources to develop and is susceptible to the greatest variance.

Batteries have a theoretical capacity that is a function of chemical composition, geometry, and temperature. However, self-discharge rates, chemical inefficiencies, and other phenomena that are temperature- and current-dependent invariably yield a reduced useful battery capacity. Small variances in the composition or manufacturing of batteries may also impact the capacity significantly, requiring a new set of tests in order to re-model the cell. At the moment there is no guideline for tests that will deliver the necessary information to produce a reliable model. In addition, there is no current metric for model reliability. This section describes an approach for modeling effective battery capacity using data mining and trend identification techniques on an otherwise very limited set of SubC cell test data.

## 5.5 Existing SubC Battery Capacity Data

[redacted]


(a) THQR Tool Consumption

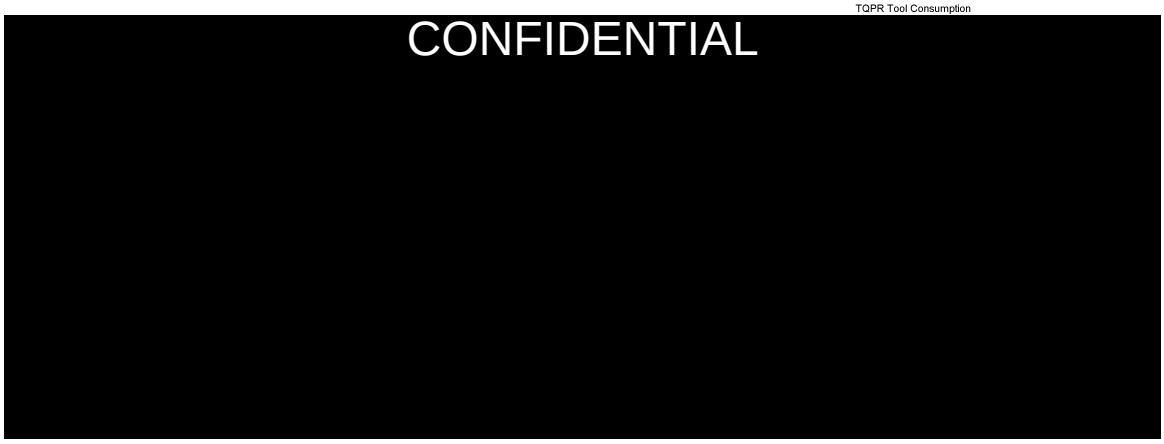


(b) TQPR Tool Consumption

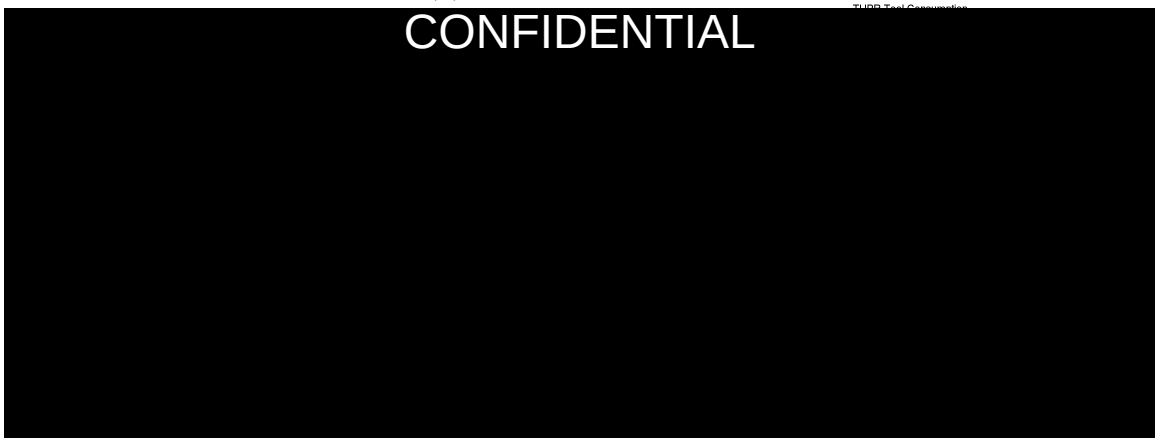


(c) TUPR Tool Consumption

Figure 25: Tool consumption as a function of sample rate and temperature for (a) THQR, (b) TQPR, and (c) TUPR gauges. The first column figures are 3D surfaces that are represented as consumption contours in the second column. Contour labels represent current load (mA).

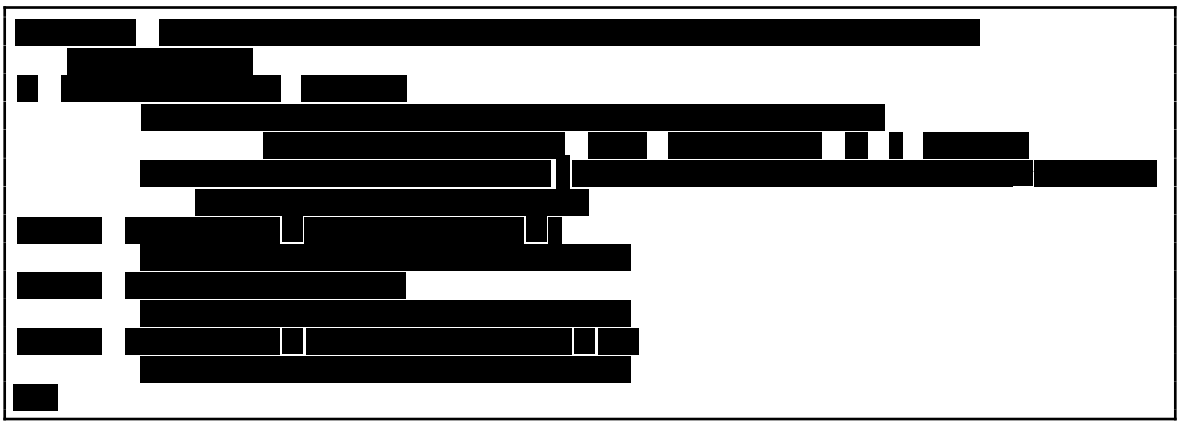

Figure 26: Pseudo-code of tool consumption for a given sample rate and temperature.

Table 13: Documented Battery Capacity and Compatibility

| | Theoretical Capacity | THQR Test | TQPR Test | TUPR Test |
|---|---|---|---|---|
| SubC 150 | | | | |
| SubC 175 | | | | |
| SubC 210 | | | | |

Table 14: Autonomy Tests for SubC DUTs

| SubC 150 | SubC 175 | SubC 210 |
|---|---|---|
| [redacted] | [redacted] | [redacted] |
| [redacted] | [redacted] | [redacted] |
| [redacted] | [redacted] | [redacted] |

[redacted]

## *5.6 Battery Autonomy Data Visualization*

This section describes the process of visualizing the data contained in 28 DUTs to identify trends. Caution should be made in trending without a theoretical/physical

explanation; however, given that this is the first attempt to create a continuous model over rated temperatures and sample rates, no justification is provided for the suggested trends. Instead, this is an initial attempt to isolate and characterize the effect of changing a single parameter (i.e., temperature or sample rate) over the effective battery autonomy. Subsequent studies should aim to bridge the theory and empirical model.

[redacted]

- [redacted]
- [redacted]
- [redacted]
- [redacted]
- [redacted]

In order to make the information more manageable, the parameters were reduced to 3 dimensions:

- Temperature (°C),
- Duty Cycle (0–1),
- Capacity (A-hr).

The duty cycle is a mapping of the sample rate (0.1 – 600 seconds) to a ratio of the time spent in active mode over the sampling period/rate. [redacted]

Table 15: Mapping of Sample Rate to Duty Cycle

| Sample Rate (sec) | [redacted] |
|---|---|
| Duty Cycle | [redacted] |

The duty cycle is useful to relate the DUT data to the standard tool sample rates (refer to Table 15). [redacted]

Figure 27 presents the capacity as a function of temperature (top row) and duty cycle (bottom row).

## *5.7 Trends in Data*

[redacted]

### 5.7.1 Capacity as a Function of Temperature

[redacted]

Figure 27: Scatter plots of battery capacity as a function of temperature (top row) and battery capacity as a function of duty cycle (bottom row) for SubC 150, 175, and 210. Color bars represent the third dimension in each case: duty cycle (top row) and temperature (bottom row). Trend lines (black dotted lines) are included for the separate battery models. Gray dotted trend lines in top row respent the shift in capacity as the duty cycle transitions from 1 to 0.083.

[redacted]

### 5.7.2 Capacity as a Function of Duty Cycle

[redacted]

[redacted]

## 5.8 Effective Battery Capacity Model

The rotation of the duty cycle vs. capacity trend line as a function of temperature was used to create a capacity surface that was a function of temperature and duty cycle or, equivalently, sample rate. This surface was then scaled by the envelope trend line limits on the duty cycle range of 0.083 – 1 at each temperature (Figure 27, top row).

In addition to tool consumption measurements and effective battery capacity to model the tool autonomy, a monthly self-discharge of 3% of the capacity was incorporated into the model to account for discharge rates over prolonged use of Lithium batteries. [redacted]

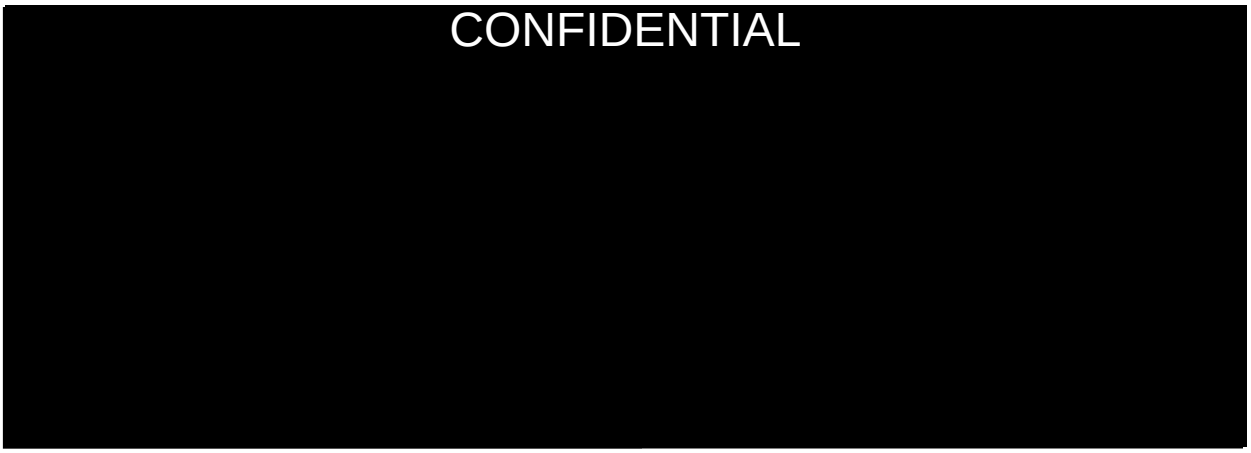


(a) SubC 150 Cell


(b) SubC 175 Cell


(c) SubC 210 Cell

Figure 28: Effective battery capacity as a function of sample rate / duty cycle and temperature [redacted] The 3D surfaces on the first column are represented as capacity contours in the second column. Colour labels represent capacities (A-hr).

## 5.9 Tool Autonomy

The effective battery capacity (in Figure 28) is divided by the tool consumption (in Figure 25) to produce memory-less tool autonomy, per Eq. 28. At each temperature and sample rate, this estimated tool autonomy (based on battery capacity and tool consumption) is compared to the memory autonomy. The lesser of the two autonomies determines the final tool autonomy. The final tool autonomy model is illustrated in Figure 29 for THQR/TQPR/TUPR on compatible SubC cells.

Tables summarizing the results in Figure 29 are included in Appendix D.1. These tables include autonomies for standard sample rates at temperature intervals that are useful to field operators.

## 5.10 Recommended Autonomy Measurement Campaign

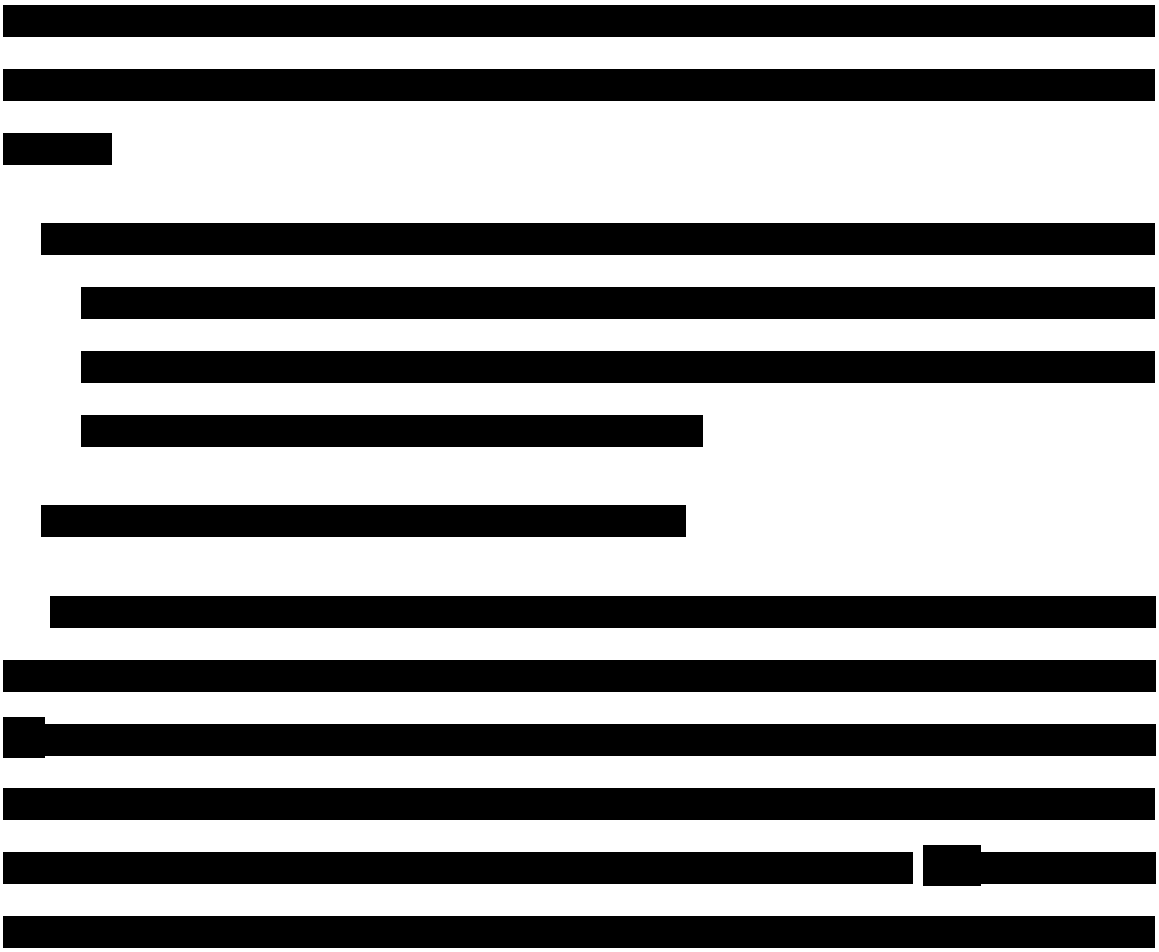


(a) THQR - SubC 150 (b) TQPR - SubC 150


(c) THQR - SubC 175 (d) TQPR - SubC 175


(e) THQR - SubC 210 (f) TUPR - SubC 150

Figure 29: Tool autonomies for (a)/(c)/(e) THQR, (b)/(d) TQPR, and (f) TUPR using compatible SubC cells. [redacted]


Figure 30: Recommended temperature and sample rates for battery DUT capacity tests (non-solid markers). Existing DUTs listed in Appendix D.2 are also included (solid markers).

[redacted]

Table 16: Autonomy Characterization Strategy for Signature™ Battery Packs [4]

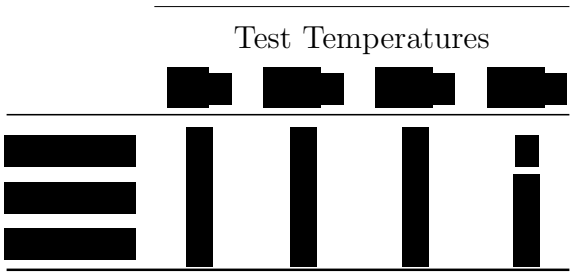


## *5.11 Future Tests*

# CHAPTER VI

# CONCLUSION

This monograph provides a detailed account of four related, albeit independent, problems in the area of downhole pressure gauges. While the material focuses namely on high-pressure, high-temperature gauge metrology, autonomy, and signal processing, the concepts are generalizable and the methods can be applied to a broader range of tools, processes, and applications.

In Chapter 2, the reader is equipped with the response surface methodology required to calibrate quartz pressure gauges. After verifying that the errors associated with the calibration process are normally distributed, an unpaired sample statistic is introduced and an estimate model is proposed that relates an absolute and relative accuracy of two gauges to their calibration mean quadratic deviation ($MQD$). The methodology of the unpaired sample statistic is found to reduce the uncertainty in gauge metrology, improving the absolute tool accuracy by 33% and the relative tool accuracy by 56%.

With the case study, a new metric that relies on coupled gauge performance helps define a stable pressure regime. With the new regime of stability, a metric described as "onset of stability" helps quantify the transient between a DST shut-in and the moment gauges begin to record within specification. As an addendum, the unpaired sample statistic methodology is provided as a means of evaluating not only tools, but also existing calibration processes to compensate or optimize them. Additional research is proposed to further reduce the uncertainty in gauge metrology by shifting to the paired sample statistic.

With knowledge of the calibration process, Chapter 3 revisits the response surface

methodology and evaluates the effects of removing subsets of calibration points. In brief, points that are considered unrealistic in oil exploration are removed from the coefficient matrix calculation. Unrealistic points are concentrated at low pressures and at high pressures in low temperatures. A new metric, based on the response surface subsets, is defined to quantify the $MQD$ limited to those the calibration space: $MQD_{Sub}$. Finally, the subset that removes both low pressure and low pressure, high temperature calibration points not only reduces calibration time by a factor of 1.3, but also improves calibration accuracy by 14.1%.

The challenge of memory gauge signal alignment, which is introduced briefly in the treatment of field data in Chapter 2, is developed in Chapter 4. The chapter offers a robust method of aligning pressure and temperature signals from memory gauges through a dynamic time warp (DTW) algorithm. The chapter presents a discussion on the benefits of optimizing the näive DTW and provides the framework to the DTW algorithm that is capable of aligning excessive, non-linear misalignments in memory gauge data. Future work should focus on automating the DTW tuning parameter estimation. Suggested improvements on a future DTW algorithm include a hybrid model and faster implementation to reduce memory requirements on high-resolution alignments.

Finally, Chapter 5 proposes a method to model tool autonomy by treating the battery capacity and tool consumption models independently of each other. A model of battery capacity and tool consumption is developed for different battery packs and tools, respectively, using disparate historical test data. Based on these two models, an empirical tool autonomy model is presented. Given the time and cost incurred by battery capacity tests, a response surface methodology is proposed that can leverage existing data with new test data to produce a more reliable tool autonomy model. The proposed design of experiments also reduces the number of autonomy experiments required for a thorough model by a factor of 1.5.

# APPENDIX A

# CALIBRATION AND CALIBRATION CHECK ERROR DATA

## *A.1 Distribution of Errors in Calibration*

The distribution of the collective errors for 31 unique gauge calibrations and 10 unique gauge calibration checks. Figure 31 provides qualitative evidence of bell-shaped distribution for the errors in calibration processes. The t-test's requirements on skewedness, unimodality, and sample size ($n > 16$) can also be qualitatively confirmed in Figure 31.

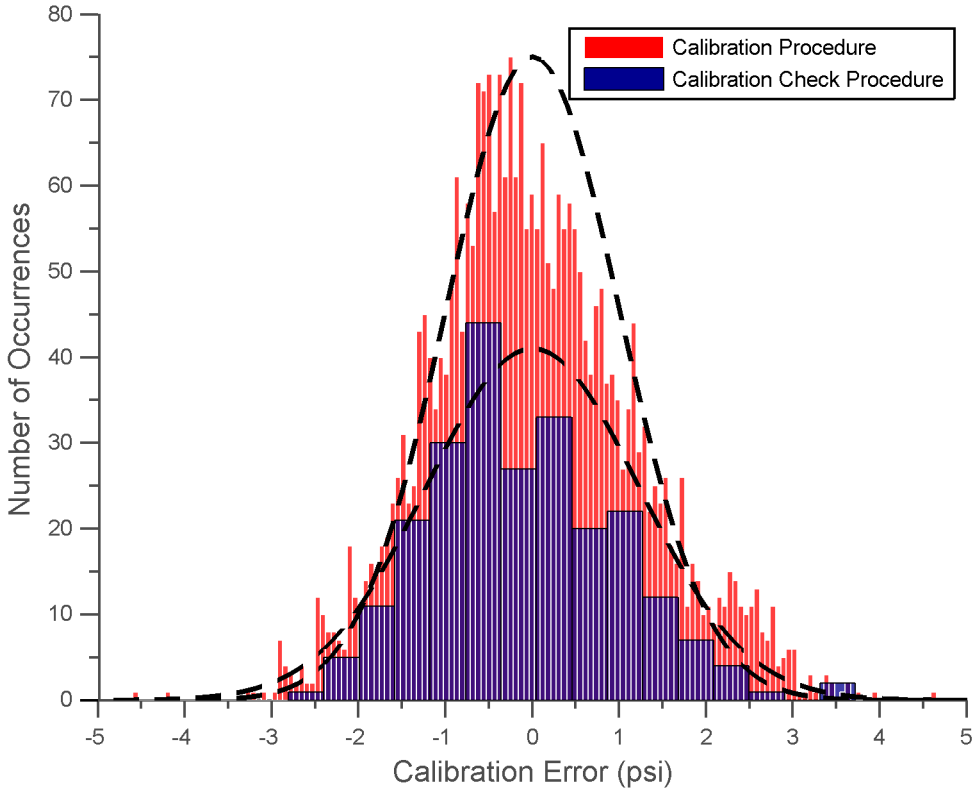


Figure 31: Bell-curve distribution of errors in gauge calibration and calibration check.

# APPENDIX B

# HISTORICAL THQR GAUGE PERFORMANCE CONDITIONS AND POTENTIAL WEIGHT FUNCTION FOR CALIBRATION POINTS

Historical data from 13 THQR gauges. The weight surfaces are based on histograms of the historical pressure/temperature events as well as from recommendations from downhole gauge engineers.

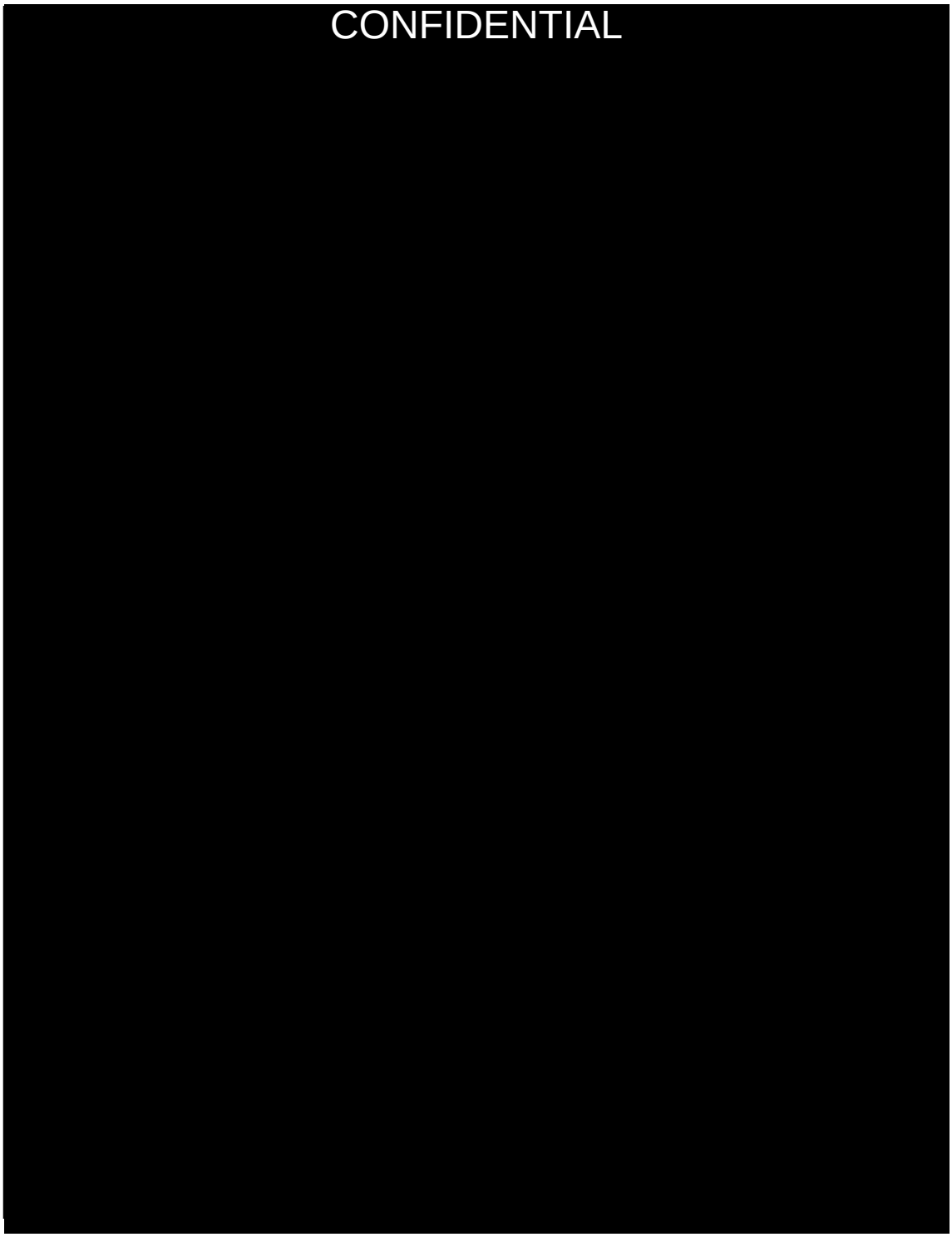


Figure 32: Superposition of historical THQR data with suggested weight surface for calibration of points. Low temperatures at pressures under 15 Kpsi are fully included in this weight model.

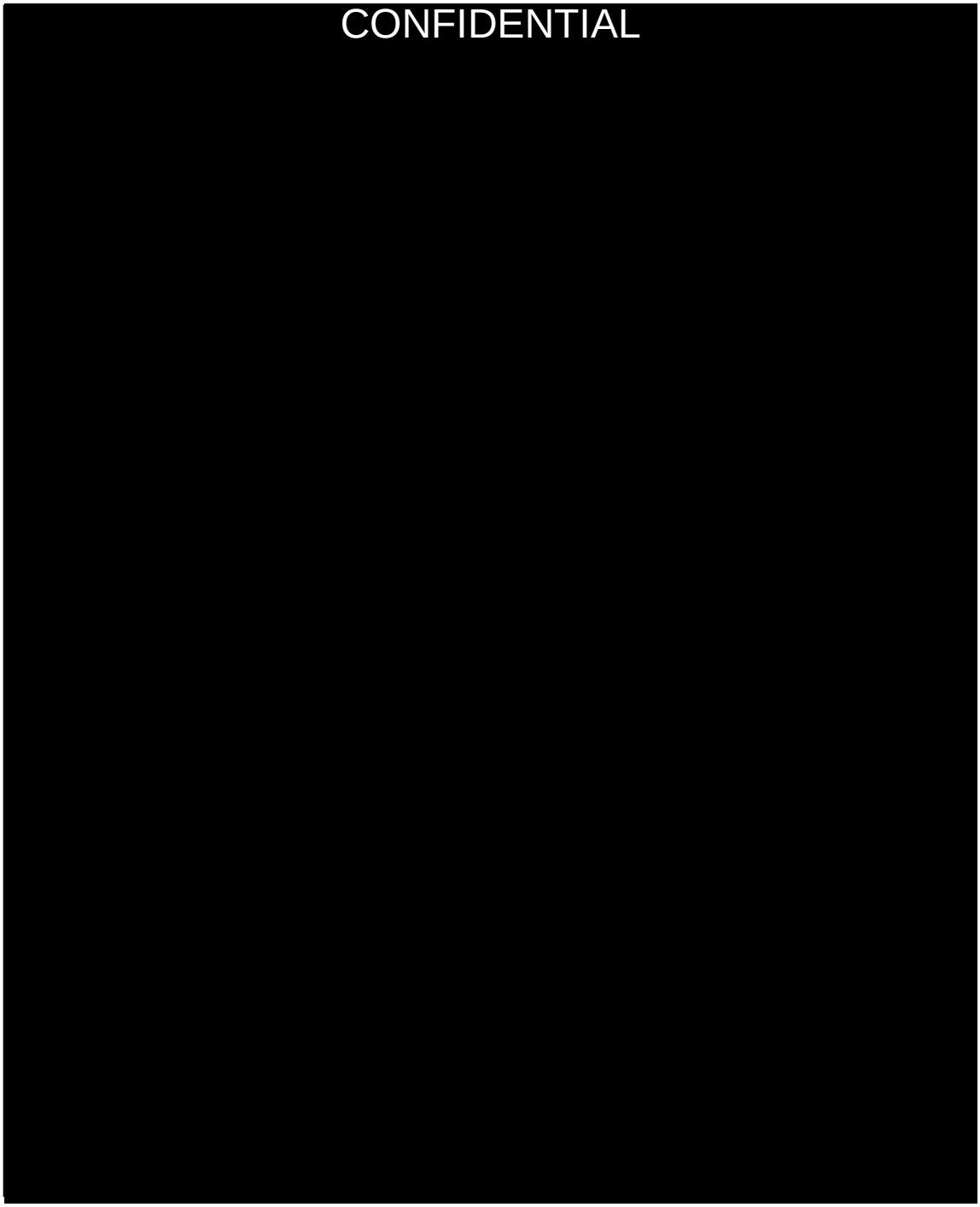


Figure 33: Superposition of historical THQR data with suggested weight surface for calibration of points. Low temperature points have an exponentially decaying weight with growing pressure. Ambient temperature and atmospheric pressure is fully weighted.

# APPENDIX C

# 2D FITTING USING LEGENDRE POLYNOMIALS IN MATLAB

Software in MATLAB for a two dimensional fitting using Legendre polynomials

## *C.1 Extracting data from Schlumberger calibration sheets and calculation of performance metrics*

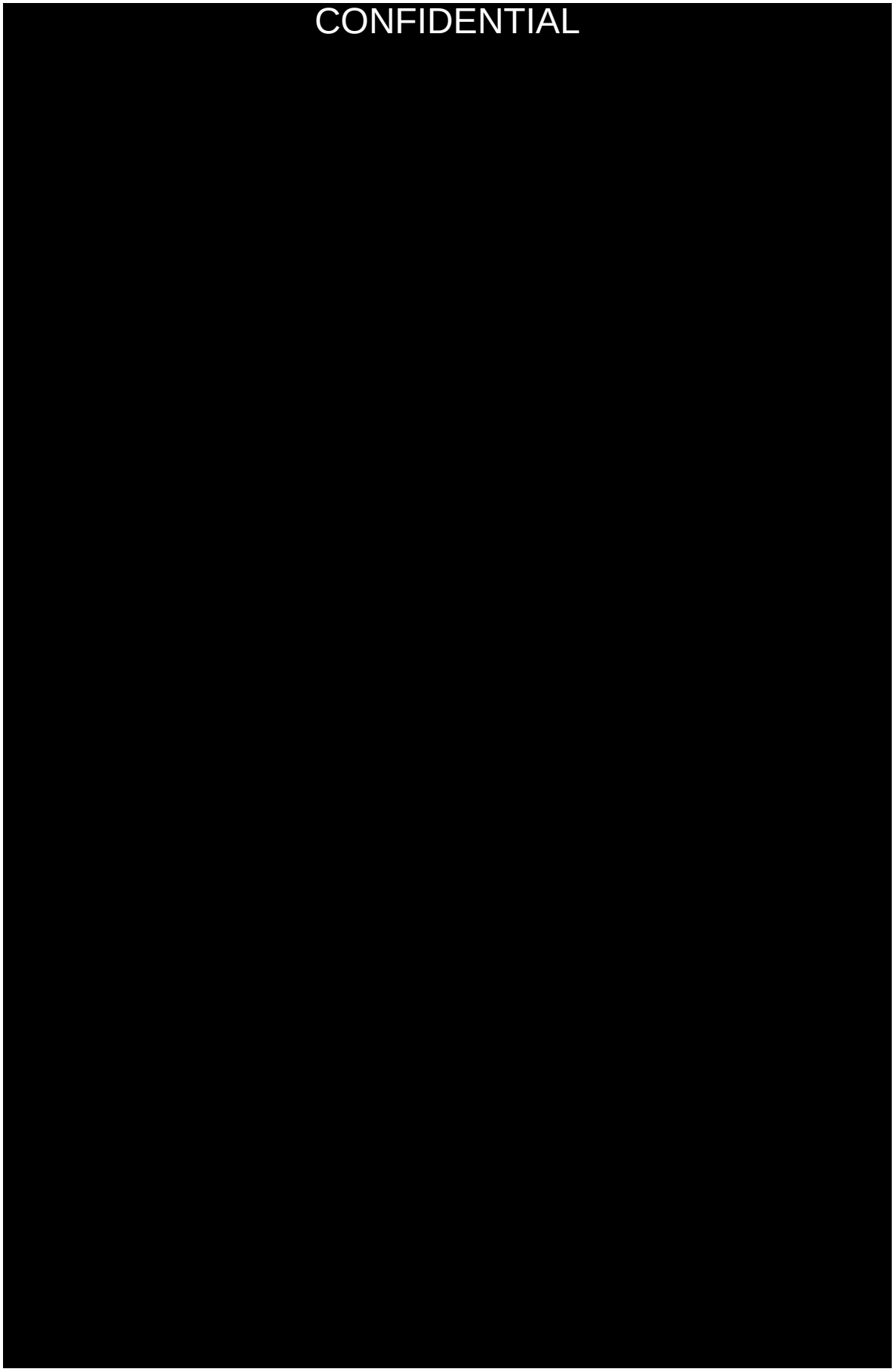

CONFIDENTIAL

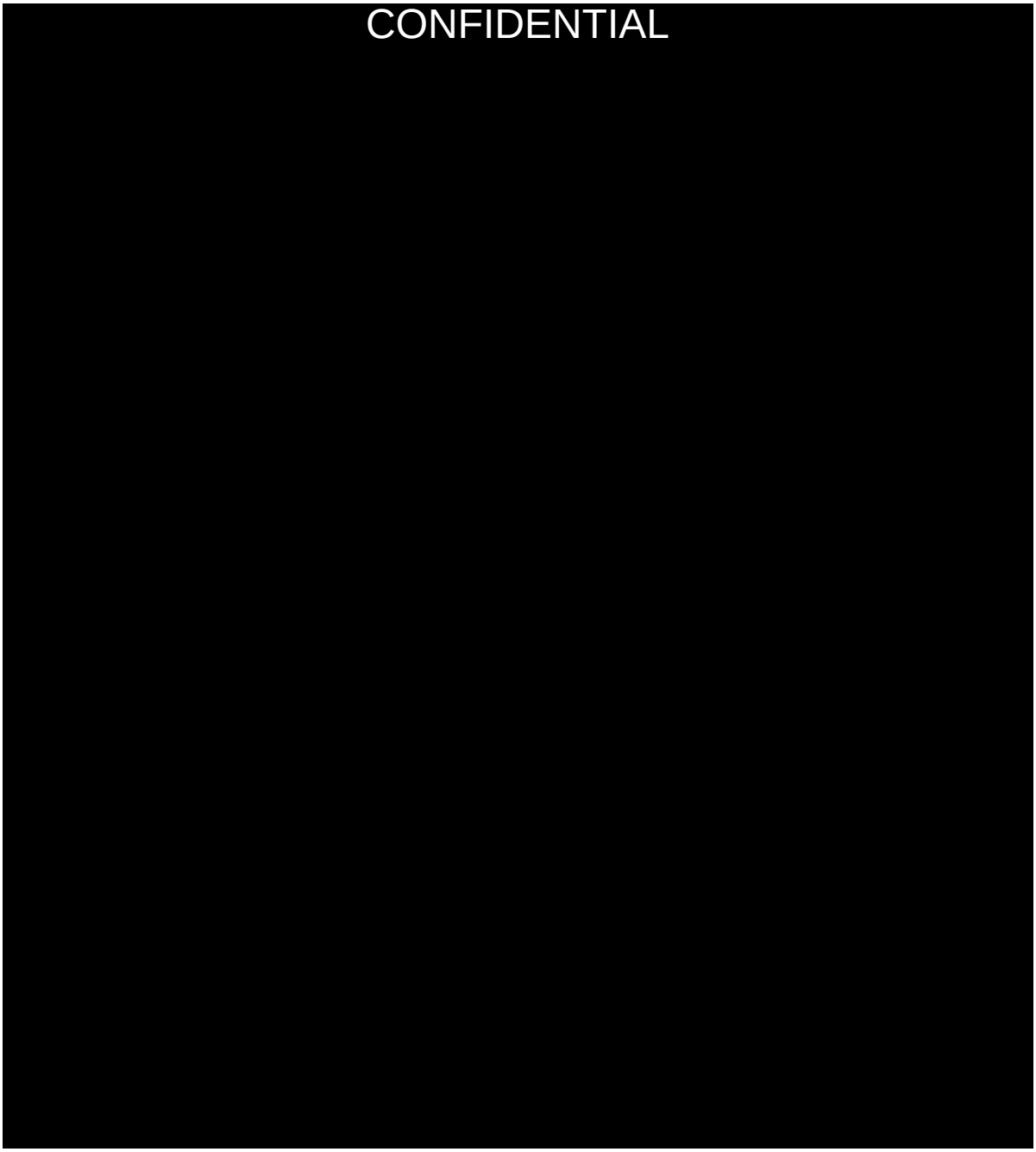


### *C.2 Linear mapping of a vector to range of* $[-1, +1]$


### *C.3 Producing normalized Legendre polynomial coefficients*

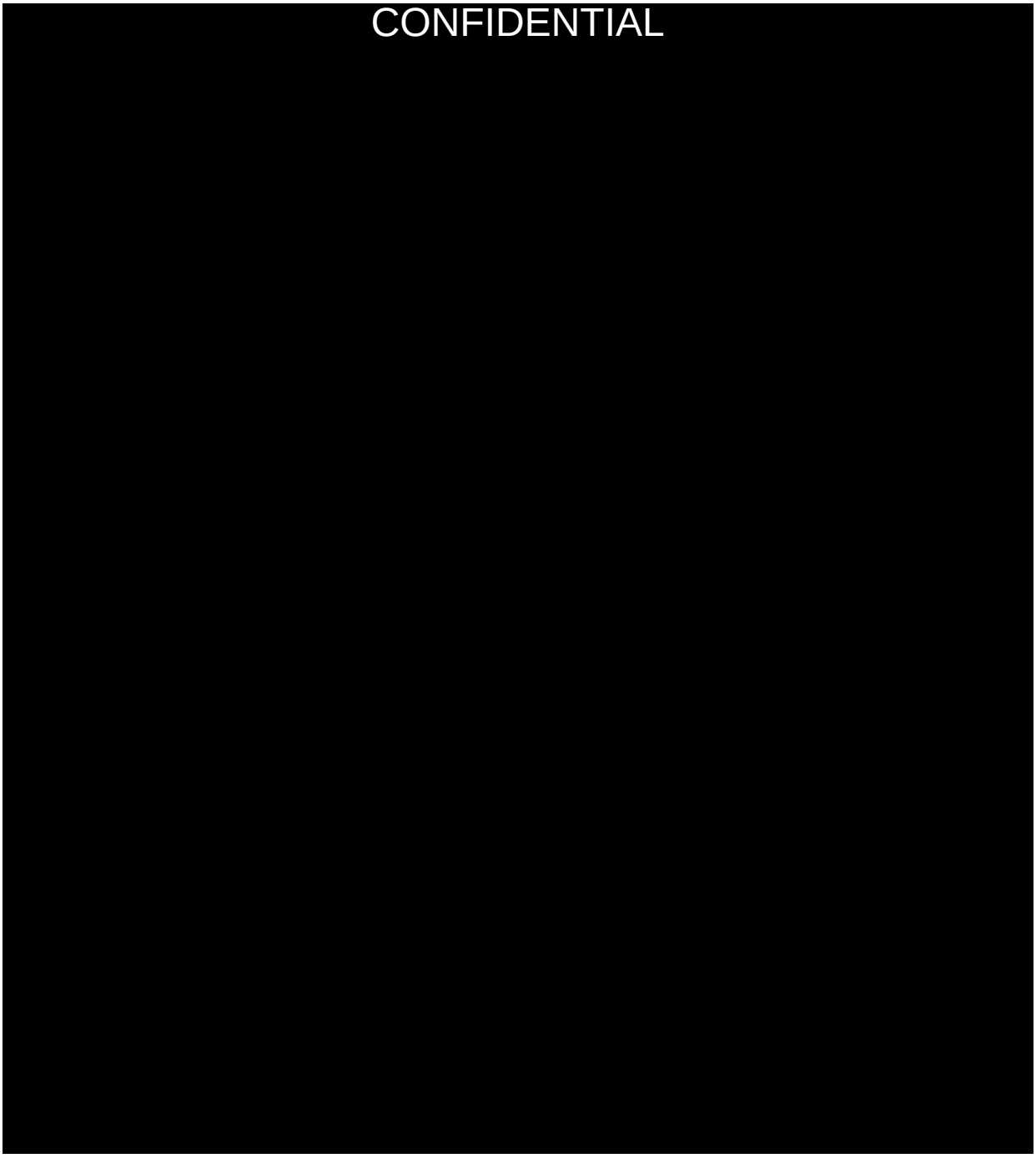


### *C.4 Reproducing vector results in matrix form*

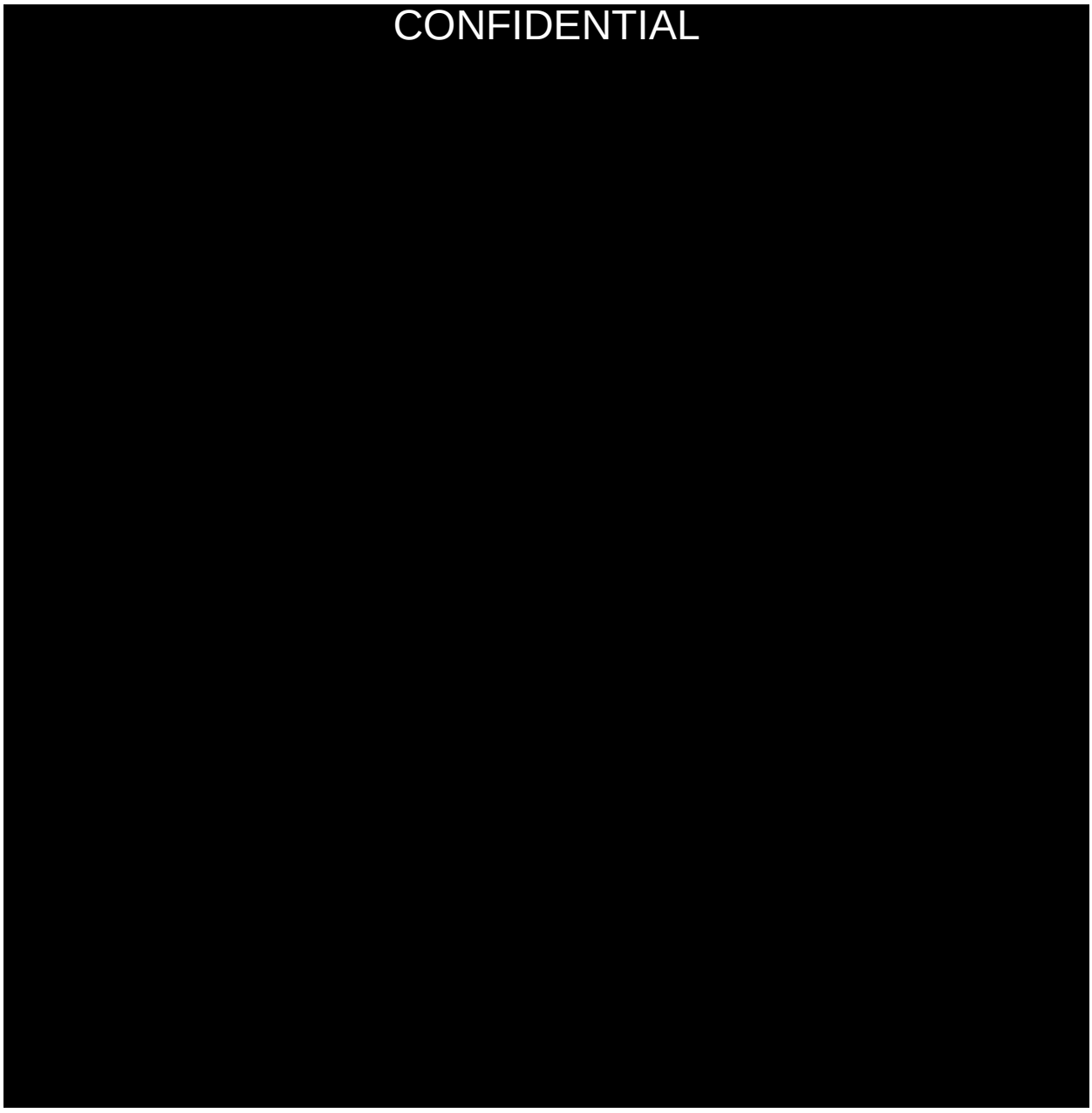


### *C.5 Look-up table of order of 2D polynomial to calculate coefficient matrix*


CONFIDENTIAL

# APPENDIX D

# TOOL AUTONOMY DATA

## *D.1 Tool Autonomy Tables*

The following autonomy tables are extracted from the tool autonomy surfaces in Figure 29. Sample rates and temperatures of interest are included; these tables are primarily for use by field operators to select appropriate tool and battery models for the job. These tables are included in the manual: VOL 1 THQR-BA/BB TQPR-BA.

### D.1.1 Table of Autonomy of THQR-B/C and A with ASIC C using SubC 150/175/210

Table 17: THQR with SubC 150 Battery Autonomy (days)

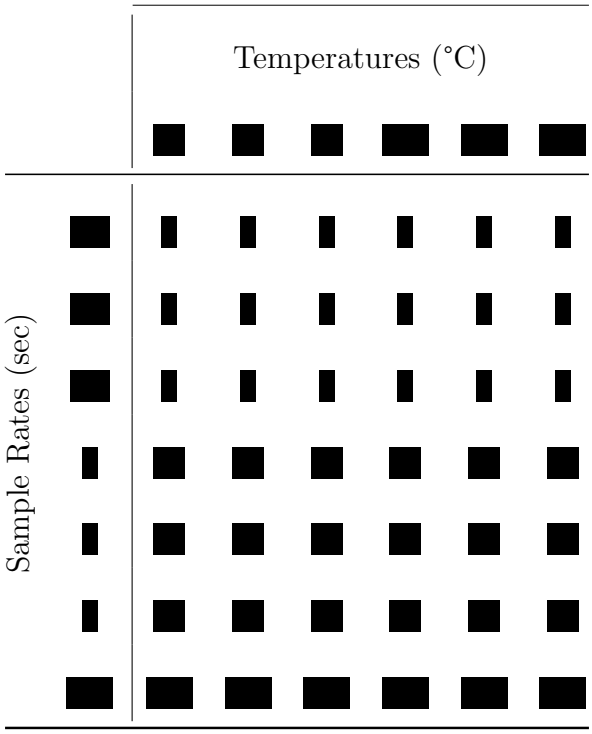

Table 18: THQR with SubC 175 Battery Autonomy (days)

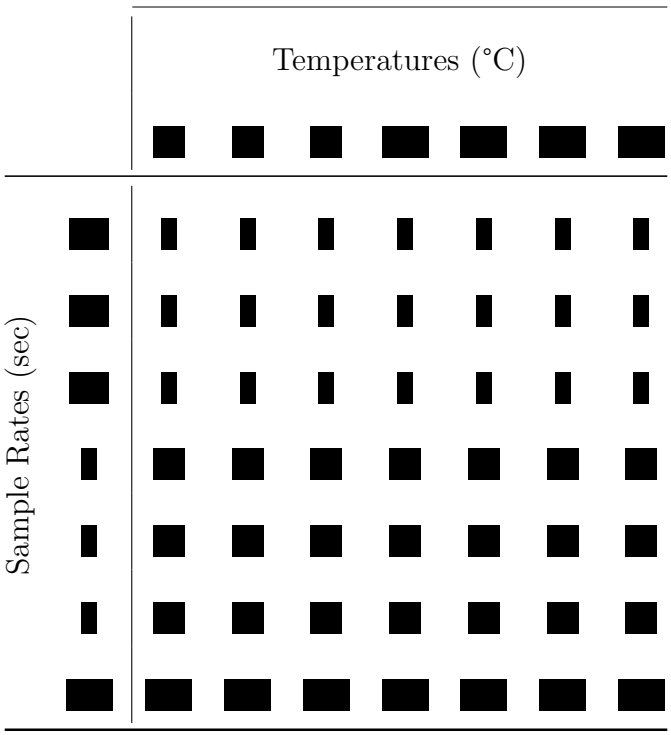

Table 19: THQR with SubC 210 Battery Autonomy (days)

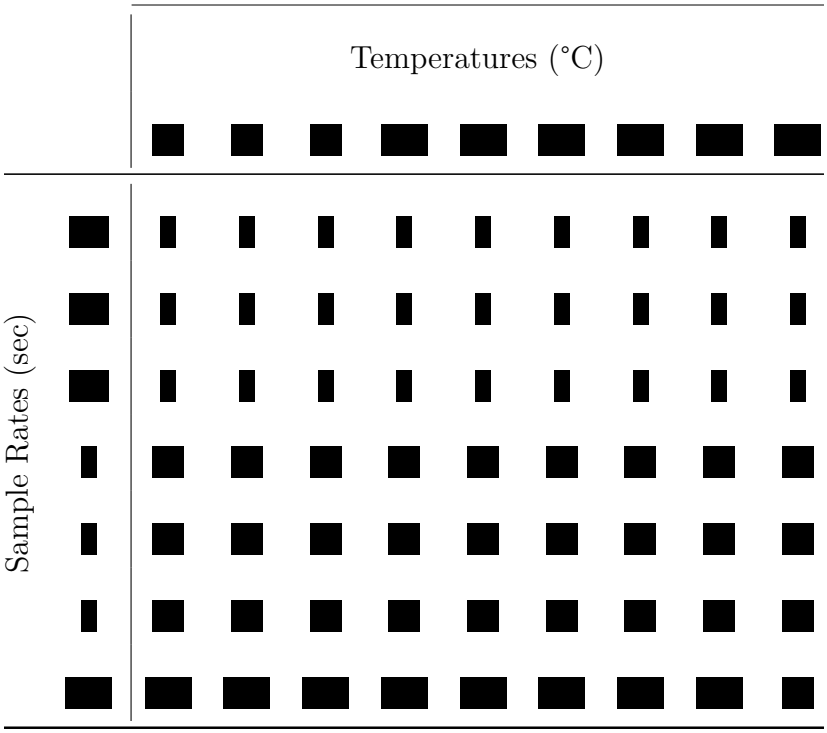

### D.1.2 Table of Autonomy of TQPR-A/BA with ASIC C/D using SubC 150/175

Table 20: TQPR with SubC 150 Battery Autonomy (days)

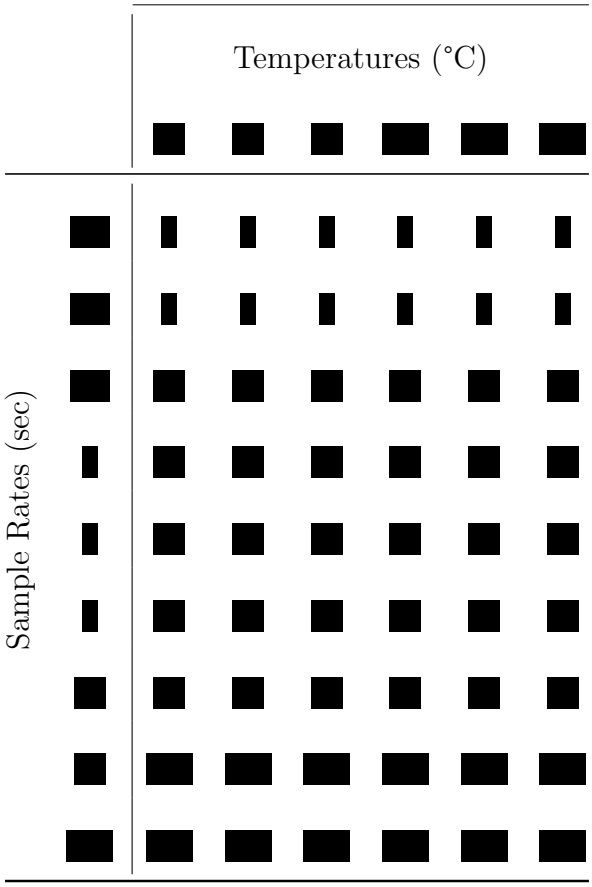

Table 21: TQPR with SubC 175 Battery Autonomy (days)

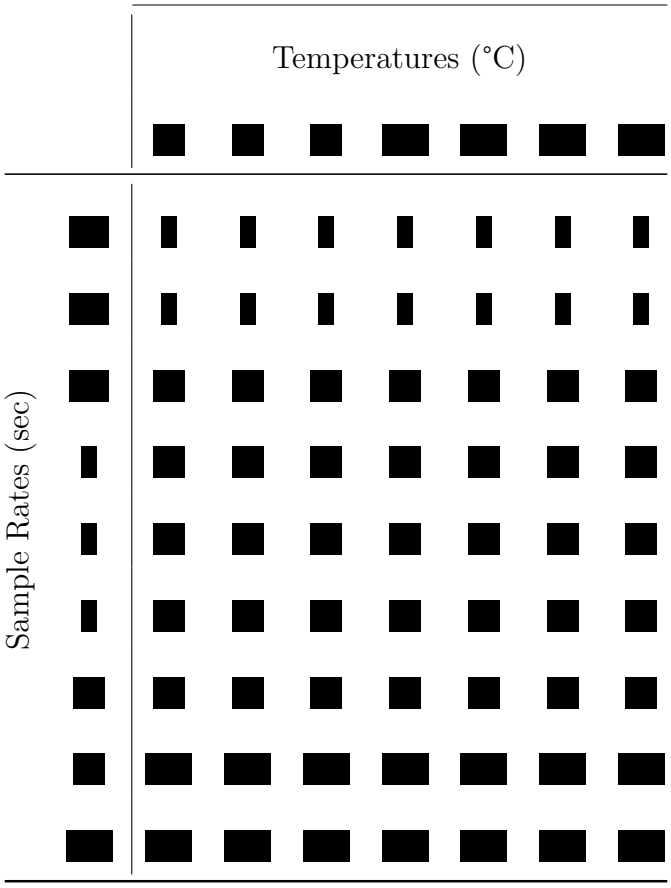

### D.1.3 Table of Autonomy of TUPR-A with ASIC D using SubC 150

Table 22: TUPR with SubC 150 Battery Autonomy (days)

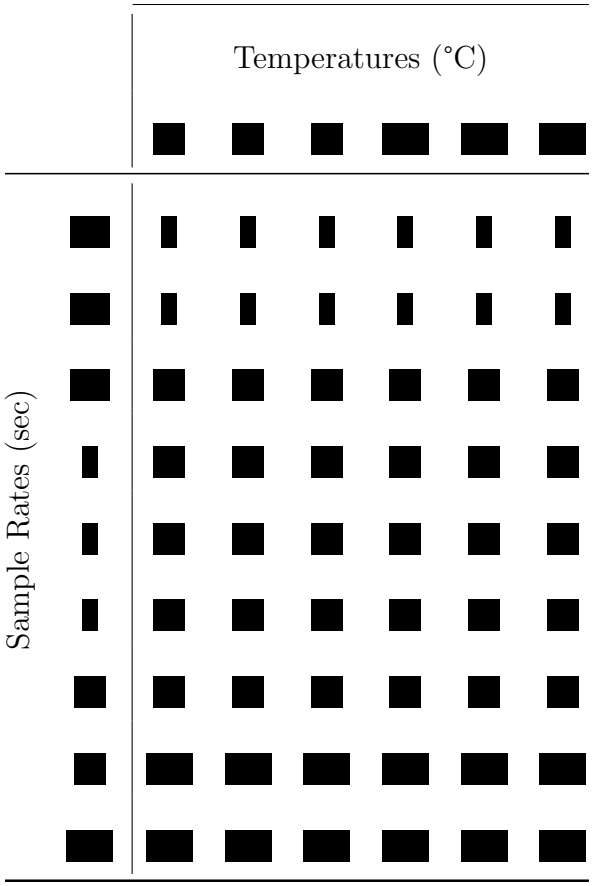


## *D.2 Documented Tests of Autonomy of SubC 150/175/210 Cells*

Table 23: Documented Autonomy Tests for SubC 150/175/210 Cells

# References


[1] "Signature quartz gauges: Reliable, accurate pressure measurements in extreme environments," tech. rep., Schlumberger, 2011. Web resource, available: http://www.slb.com/Signature.

[2] Adekanmbi, J., "Battery table." Battery Table in SharedPoint under EMS-DT/NPD/NewGauges/Field Documentation and Training. CONFIDENTIAL.

[3] Adekanmbi, J., "25% mg sub-c cell autonomy test at 205 and 210°c for jackdaw," Test Plan / Report ET201010237 / 100873528, Stonehouse Technology Center, Stonehouse, United Kingdom, Jan 2011. PRIVATE.

[4] Adekanmbi, J., "Autonomy characterization strategy: 150, 175 & 210°c signature test," Test Plan / Report ET201110028 / ET201108540 / GeMS 100989906, Stonehouse Technology Center, Stonehouse, United Kingdom, May 2012. PRIVATE.

[5] Adekanmbi, J., Graham, J., and Gunney, R., "Sub-c cell autonomy test at 0-60 and 125°c for kaskida operation," Test Plan / Report ET201002982 / 100792877, Stonehouse Technology Center, Stonehouse, United Kingdom, Jul 2010.

[6] Buisson, A., "Study of two dimensional polynomial fitting," Memo-to-File 7730-103002, Schlumberger Pressure Sensors, Clamart, France, Jan 2006. Project Manager: F. Rezgui. Document called totopolyenglish.doc.

[7] Cismondi, F., Fialho, A. S., Vieira, S. M., Sousa, J. M. C., Reti, S. R., Howell, M. D., and Finkelstein, S. N., "Computational intelligence methods for processing misaligned, unevenly sample time series containing missing data," in *2011 IEEE Symposium on Computational Intelligence and Data Mining (CIDM)*, (Paris, France), pp. 224 – 231, Engineering Systems Division, Massachusetts Institute of Technology, Apr 2011.

[8] Diniz, A. C. G. C., Oliveira, A. B. S., ao Nildo de Souza Vianna, J., and Neves, F. J. R., "Dynamic calibration methods for pressure sensors and development of standard devices for dynamic pressure," *XVIII IMEKO World Petroleum Congress*, Sep 2006.

[9] Duda, R. O. and Hart, P. E., *Pattern Classification and Scene Analysis*. New York: John Wiley & Sons, first ed., Feb 1973.

[10] Filos, J., "Time-domain alignment of non-stationary signals," Master's thesis, Imperial College London, England, Jun 2007.

[11] Fragkou, P. and Petridis, V., "Segmentation of greek text by dynamic programming," in *Proceedings of the 19th IEEE International Conference on Tools*

*with Artificial Intelligence*, vol. 2 of *ICTAI '07*, (Washington, DC, USA), pp. 370–373, IEEE Computer Society, 2007.

[12] Fu, A. W.-C., Keogh, E., Lau, L. Y. H., Ratanamahatana, C. A., and Wong, R. C.-W., "Scaling and time warping in time series querying," *Proceedings of the 31st International Conference on Very Large Data Bases*, pp. 649 – 660, Sep 2005.

[13] Group, B., "100% li sub-c cells and 10% mg," Technical Memo 100775467 / 100279559, Stonehouse Technology Center, Stonehouse, United Kingdom.

[14] Hailstone, J. and Ovens, J., "Do electronic pressure gauges have 20/20 vision?," *SPE Annual Technical Conference and Exhibition*, Oct 1995. Paper SPE 30614. DOI: 10.2118/30614.

[15] Henniger, O. and Muller, S., "Effects of time normalization on the accuracy of dynamic time warping," *First IEEE International Conference on Biometrics: Theory, Applications and Systems*, pp. 1 – 6, Sep 2007.

[16] Horne, R. N., *Modern Well Test Analysis: A Computer-Aided Approach*. Palo Alto, CA: Petro Way, second ed., Dec 1996.

[17] Jackson, R. R., Carnegie, A., and Dubost, F. X., "Pressure measurement and pressure gradient analysis: How reliable for determining fluid density and compositional gradients," *Nigeria Annual International Conference and Exhibition*, Aug 2007. Paper SPE 111911. DOI: 10.2118/111911-MS.

[18] Janssen, E. and Wahby, A., "Battery cell evaluation for new pressure recorder," Test Plan / Report ET200603240 / 100333958, Schlumberger Riboud Product Center WCP Testing, Clamart, France, Apr 2009.

[19] Kabir, C. S. and Pop, J. J., "How reliable is fluid gradient in gas/condensate reservoirs?," *SPE Gas Technology Simposium*, May 2006. Paper SPE 99386. DOI: 10.2118/99386-PA.

[20] Keogh, E. and Ratanamahatana, C. A., "Exact indexing of dynamic time warping," *Knowledge and Information Systems*, vol. 7, pp. 358 – 386, Mar 2005.

[21] Kikani, J., Fair, P. S., and Hite, R. H., "Pitfalls in pressure gauge performance," *SPE Annual Technical Conference and Exhibition*, Oct 1997. Paper SPE 30613. DOI: 10.2118/30613-PA.

[22] Kusters, J. A. and Kaitz, G. S., "Characteristics of natural, swept natural, and cultured x and z growth quartz material in high temperature, high stress applications," *Proceedings of the Annual IEEE International Frequency Control Symposium*, 1985. DOI: 10.1109/FREQ.1985.200848.

[23] Lilliefors, H., "On kolmogorov smirnov test for normality with mean and variance unknown," *Journal of the American Statistical Association*, vol. 62, no. 318, pp. 399 – 402, 1967.

[24] Morrissey, N. and Adekanmbi, J., "Cell, sub-c, 25% mg, 210c," Drawing T6017293D, Stonehouse Technology Center, Stonehouse, United Kingdom, Nov 2010. CONFIDENTIAL.

[25] Morrissey, N. and Raezer, S., "Cell, subc, 175c," Drawing T6017192D, Stonehouse Technology Center, Stonehouse, United Kingdom, Aug 2007. CONFIDENTIAL.

[26] Morrissey, N. and Yaalaoui, M. E., "Cell, 150c, irdv," Drawing 156432D, Stonehouse Technology Center, Stonehouse, United Kingdom, May 2006. CONFIDENTIAL.

[27] Munich, M. E. and Perona, P., "Continuous dynamic time warping for translation-invariant curve alignment with applications to signature verification," in *Proceedings of 7th International Conference on Computer Vision*, pp. 108–115, 1999.

[28] Omotosho, R. J., "Permanent downhole sensors in today's petroleum industry: Current trends, problems and case studies," Master's thesis, University of Texas at Austin, Austin, TX, Aug 2004.

[29] Sakoe, H. and Chiba, S., "Dynamic programming algorithm optimization for spoken word recognition," *IEEE Transactions on Acoustics, Speech and Signal Processing*, vol. 26, pp. 43 – 49, Feb 1978.

[30] Salvador, S. and Chan, P., "Toward accurate dynamic time warping in linear time and space," *Intelligent Data Analysis*, vol. 11, pp. 561–580, Oct. 2007.

[31] Schultz, R. L. and Chen, D., "Dynamic neural network calibration of quartz transducers," *SPE Annual Technical Conference and Exhibition*, Oct 2003. Paper SPE 84381. DOI: 110.2118/84381-MS.

[32] Senin, P., "Dynamic time warping algorithm review." http://csdl.ics.hawaii.edu/techreports/08-04/08-04.pdf, Dec 2008.

[33] Vardeman, S. B., Hamada, M. S., Burr, T., Morris, M., Wendelberger, J. R., Jobe, J. M., Moore, L. M., and Wu, H., "An introduction to statistical issues and methods in merology for physical science and engineering." submitted, Sep 2011.

[34] Vardeman, S. B. and Jobe, J. M., "Statistical methods for quality assurance: Basics, measurement, control, capability, and improvement." Sep 2007.

[35] Vardeman, S. B., Wendelberger, J. R., Burr, T., Hamada, M. S., Moore, L. M., Jobe, J. M., Morris, M. D., and Wu, H., "Elementary statistical methods and measurement error," *The American Statistician*, vol. 64, pp. 46 – 51, Feb 2010.

[36] Veneruso, A. F., Erlig-Economides, C., and Petitjean, L., "Pressure gauge specification considerations in practical well testing," *SPE Annual Technical Conference and Exhibition*, Oct 1991. Paper SPE 22752. DOI: 10.2118/22752-MS.

[37] Zhou, L., Hughes, B., and Mardambek, J., "Reservoir fluid evaluationfrom real time pressure gradient analysis: Discussion on principles, workflow, and applications," *SPE Asia Pacific Oil and Gas Conference and Exhibition*, Oct 2008. Paper SPE 115045. DOI: 10.2118/115045-MS.